Article

Current Biology

Sensorimotor Transformations in the Zebrafish Auditory System

Graphical Abstract

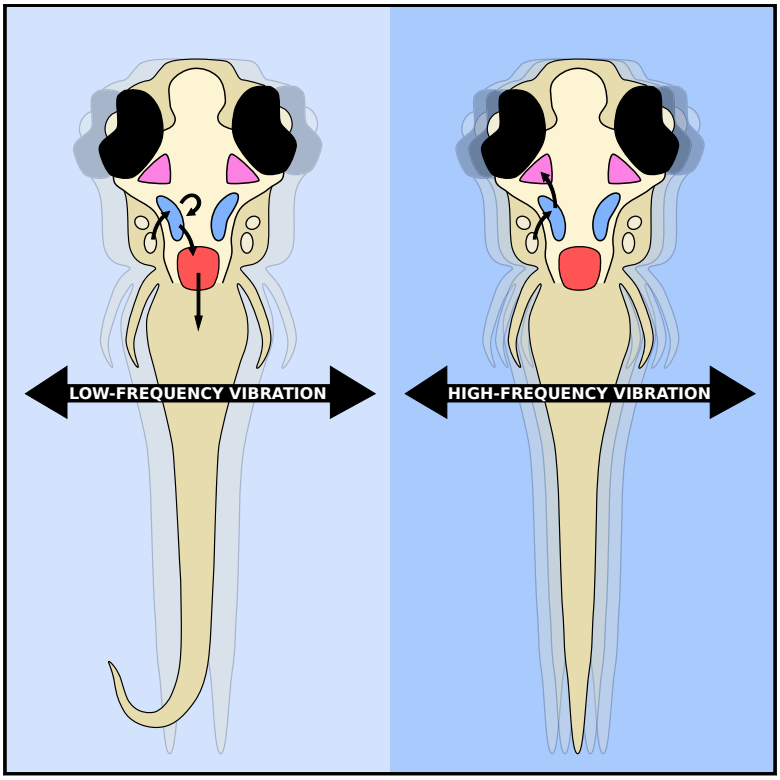

Authors

Martin Privat, Sebastián A. Romano, Thomas Pietri, ..., Auriane Duchemin, Daphne Soares, Germán Sumbre

Correspondence

sumbre@biologie.ens.fr

In Brief

How do zebrafish larvae use auditory information to generate behavior? Privat et al. show that sensorimotor transformations are represented in a topographically continuous manner. The auditory response is temporally integrated to improve the extraction of sensory information and adapt the motor response to the auditory changes in the environment.

Highlights

- Representation of sound frequencies in the zebrafish brain is low dimensional
- Low frequencies are processed in the hindbrain and induce tail movements
- High frequencies are represented in the hindbrain and midbrain
- Auditory stimuli are temporally integrated to generate tail movements

Privat et al., 2019, Current Biology *29*, 1–14
December 2, 2019
https://doi.org/10.1016/j.cub.2019.10.020

CellPress

Please cite this article in press as: Privat et al., Sensorimotor Transformations in the Zebrafish Auditory System, Current Biology (2019), https://doi.org/10.1016/j.cub.2019.10.020

Current Biology
Article

Sensorimotor Transformations in the Zebrafish Auditory System

Martin Privat,[1] Sebastián A. Romano,[1,2,7] Thomas Pietri,[1,6,7] Adrien Jouary,[1,3] Jonathan Boulanger-Weill,[1,4] Nicolas Elbaz,[1] Auriane Duchemin,[1] Daphne Soares,[5] and Germán Sumbre[1,8,*]

[1]Institut de Biologie de l'ENS (IBENS), Département de Biologie, École Normale Supérieure, CNRS, INSERM, Université PSL, 75005 Paris, France

[2]Instituto de Investigación en Biomedicina de Buenos Aires (IBioBA) – CONICET - Partner Institute of the Max Planck Society, Godoy Cruz 2390, C1425FQD Buenos Aires, Argentina

[3]Champalimaud Research, Champalimaud Centre for the Unknown, Lisbon 1400-038, Portugal

[4]Department of Molecular and Cellular Biology, Center for Brain Science, Harvard University, Cambridge, MA, USA

[5]Department of Biological Sciences, New Jersey Institute of Technology, Newark, NJ 07102, USA

[6]Present address: *Cell Reports*, Cell Press, 1043NX Amsterdam, the Netherlands

[7]These authors contributed equally

[8]Lead Contact

*Correspondence: sumbre@biologie.ens.fr

https://doi.org/10.1016/j.cub.2019.10.020

SUMMARY

Organisms use their sensory systems to acquire information from their environment and integrate this information to produce relevant behaviors. Nevertheless, how sensory information is converted into adequate motor patterns in the brain remains an open question. Here, we addressed this question using two-photon and light-sheet calcium imaging in intact, behaving zebrafish larvae. We monitored neural activity elicited by auditory stimuli while simultaneously recording tail movements. We observed a spatial organization of neural activity according to four different response profiles (frequency tuning curves), suggesting a low-dimensional representation of frequency information, maintained throughout the development of the larvae. Low frequencies (150–450 Hz) were locally processed in the hindbrain and elicited motor behaviors. In contrast, higher frequencies (900–1,000 Hz) rarely induced motor behaviors and were also represented in the midbrain. Finally, we found that the sensorimotor transformations in the zebrafish auditory system are a continuous and gradual process that involves the temporal integration of the sensory response in order to generate a motor behavior.

INTRODUCTION

One of the main goals in neuroscience is to understand how sensory information is represented in the brain and later integrated to produce relevant behaviors.

For several sensory modalities, information about the external world is represented in topographic maps. For instance, two visual stimuli that are close together in space will elicit responses in neighboring neurons (retinotopy). In mammals, birds, and lizards, acoustic frequency discrimination occurs in the cochlea due to the properties of the basilar membrane (for review, see [1]). This spatial map of the frequency spectrum on the cochlea is called tonotopy and is propagated to the CNS through parallel channels and along the auditory hierarchy up to the primary auditory areas [2–5]. Teleosts fish do not have a cochlea, but their inner ear consists of otoliths and a series of hair cells used for both the auditory and the vestibular system capable of detecting the acceleration component of sound [6]. In juveniles and adult fish, the emergence of the Weberian ossicles enables the transmission of sound pressure detected by the swim bladder to the inner earþ. In some species, this structure decreases the detection threshold and increases the sensitivity for high frequencies [7]. However, they are capable of using auditory information to detect prey, avoid predators, or to eavesdrop on animals from the same or different species [8–10]. Therefore, teleost fish should be capable of performing basic frequency discrimination at the level of the sensory hair cells or the nervous system. Indeed, frequency segregation was observed in the goldfish, where rostral saccular afferents respond to high frequencies and caudal afferents are tuned to lower frequencies [11], probably due to mechanical properties of the hair cells.

In teleost fish, the octaval column receives inputs from the primary afferents of the inner ear and projects in turn to the torus semicircularis [12]. These two regions are thought to be homologous to the mammalian cochlear nucleus and the inferior colliculus. In goldfish, crude tonotopy was reported in the torus semicircularis [13]. In zebrafish larva, a coarse spatial frequency organization was hypothesized [14, 15], but it still remains to be demonstrated.

Sensory representations are used to decode and interpret the external sensory world and generate motor patterns to respond to an ever-changing environment. For this purpose, the brain needs to compute sensorimotor transformations to convert the sensory responses into relevant motor behaviors.

Sensorimotor transformations have been studied in the context of chemotaxis and olfaction in the fruit fly [16–19] and in *C. elegans* [20, 21], active sensing and exploration [22–24], and sensorimotor learning in mice [25]. However, these studies

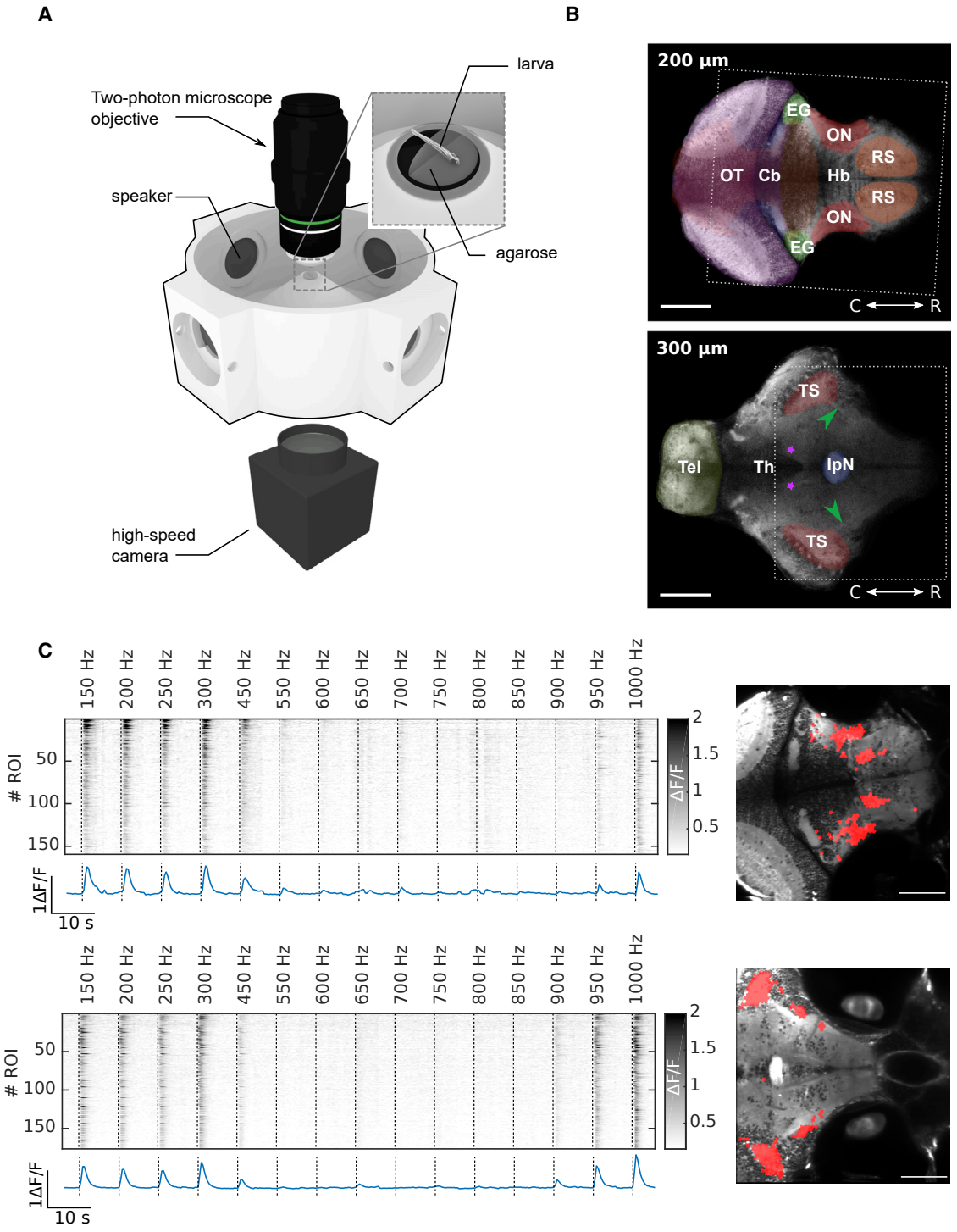

Figure 1. Experimental Setup for Acoustic Stimulation and Simultaneous Recording of Neural Activity and Behavior

(A) Zebrafish larvae were head restrained in a drop of low-melting-point agarose inside a 3D-printed recording chamber. Acoustic stimulations (pure tones at different frequencies) were delivered using waterproof speakers. Spontaneous and evoked neuronal activity was monitored by two-photon calcium imaging while movements of the tail were simultaneously recorded with a high-speed camera.

(B) Two optical sections of a larva's brain pan-neuronally expressing GCaMP5 (Huc:GCaMP5). Cb, cerebellum; EG, eminentia granularis; Hb, hindbrain; IpN, interpeduncular nucleus; ON, octaval nuclei; OT, optic tectum; RS, reticulospinal neurons; Th, thalamus; Tel, telencephalon; TS, torus semicircularis. Green

(legend continued on next page)

involve transformations at the cellular level or by monitoring a relatively small group of neurons. Using the zebrafish larva, which allows simultaneously monitoring sensory and motor circuits and motor behaviors, it is possible to study sensorimotor transformations at the circuit level [26–29]. For example, visuomotor transformations are thought to occur at a brain region in the anterior hindbrain, where several visual responses converge [28].

Despite these advances, the neuronal circuit principles and mechanisms underlying sensorimotor transformations remain elusive.

Here, we took advantage of the auditory system of the zebrafish to study sound representations in the brain and the principles underlying their transformation into motor patterns. For this purpose, we used light-sheet and two-photon calcium imaging in intact, behaving zebrafish larvae expressing the genetically encoded calcium indicator GCaMP5. We monitored neural activity elicited by pure tones (150–1,000 Hz) and broadband noise across large portions of the brain with near single-cell resolution while simultaneously recording motor activity.

We found that auditory-induced neuronal responses were spatially organized according to four main different response profiles. Low frequencies (150–450 Hz) were locally processed in the hindbrain although higher ones (900–1,000 Hz) were transferred to the midbrain, suggesting the existence of two channels for processing auditory information. We propose that the local low-frequency channel is mainly used for the generation of an adequate motor behavior, although the second channel (low and high sound frequencies) may be involved in the modulation of other sensory modalities [30].

To study how sounds are processed and transformed into motor patterns, we classified the neuronal responses according to their correlation with the auditory stimuli and the larva's tail movements. We found that auditory-induced activity propagated in the brain from sensory to motor areas via an intermediate sensorimotor circuit that was active upon the presentation of a stimulus but also during motor behaviors. Sensory networks faithfully encoded auditory information, regardless of the behavioral output, and motor networks did not show sensory-related activity. However, sensorimotor circuits were more active when a stimulus was followed by a motor behavior than in response to stimuli alone. Finally, we observed that the duration of the neuronal response was longer across the whole network when an auditory stimulus was followed by a motor behavior, suggesting that, in the auditory system of the zebrafish larva, sensorimotor transformations involve a temporal integrative process of the neuronal sensory response.

RESULTS

Auditory Responses in the Brain

To study how auditory stimuli are represented, integrated, and transformed into motor patterns in the auditory system of the zebrafish larva, we built a 3D-printed recording chamber with waterproof speakers (Visaton K28 WP) that enables delivering auditory stimuli, monitoring motor behaviors (tail movements), and recording neuronal activity using two-photon microscopy (Figure 1A). Eight days post-fertilization (dpf), transgenic zebrafish larvae expressing pan-neuronally GCaMP5 (*Huc:GCaMP5*) were restrained in low-melting agarose and placed in the center of the recording chamber. Calcium dynamics were monitored using a two-photon microscope from above the chamber. The agarose around the tail was removed, allowing monitoring the deflections of the tail using a high-speed camera (Figure 1A). Under these conditions, we presented to the larvae pure tones with frequencies ranging from 150 Hz to 1,000 Hz (STAR Methods). This range was selected based on previous studies [14, 31–33]. Due to the acoustic properties of the recording chamber and the non-linearities of the speakers, the presented auditory stimuli may have deviated from those generated by the computer. Therefore, we measured for each frequency stimulus the sound pressure and the particle acceleration within the chamber. Both pressure and acceleration were then equalized to obtain almost equal values across the frequency range used in our experiments (Figures S1B and S3B). In addition, to minimize the generation of harmonics, we used an auditory pulse with a ramping onset and a decaying offset (Figure S1A).

Neuronal activity was recorded from different optical planes containing the octaval nuclei (ON) in the hindbrain, which is the first known relay for auditory information in teleost fish; the reticulo-spinal circuit; the cerebellum; the nucleus of the medial longitudinal fascicle (nucMLF); and the torus semicircularis in the midbrain region, homologous to the inferior colliculus in mammals (Figures 1B, 6D, and 6E).

To extract regions of interest (ROIs) responsive to the auditory stimuli, we used a regression approach (STAR Methods) based on stimulus-related regressors, one for each presented frequency. We then used this series of regressors to fit a linear model to the fluorescence time series of each ROI (Figure S2). The goodness of fit was assessed by computing the percentage of variance in the time series explained by the model (R^2_{stim}). Only ROIs with high R^2 were kept for further analysis (STAR Methods). Using this approach, we found auditory-responsive ROIs in the octaval nuclei, in the eminentia granularis, in the torus semicircularis, and in a small nucleus on the lateral side of the lateral longitudinal fascicle (a total of 1,917 ROIs from 13 larvae; STAR Methods; Figure 1C).

Auditory signals convey information through their intensity, their frequency content, and their variations over time. Here, we focused on the sound frequency content, which may carry crucial information about the nature of the sound source and trigger relevant motor behaviors. For example, the largemouth bass (*Micropterus salmoides*) produces ~170 dB at ~200 Hz when feeding on guppies [34], and cyprinid fish are attracted

arrowheads, lateral longitudinal fascicle; purple asterisks, nucleus of the medial longitudinal fascicle. Scale bars, 100 μm. Dotted rectangles correspond to area displayed in (C).

(C) Two examples of sensory activity in the octaval nuclei (top) and torus semicircularis (bottom). Top: raster example for one larva averaged across trials for each stimulus frequency is shown. Bottom: activity averaged across ROIs is shown. Right: topography of ROIs selected as responsive using linear regression corresponding to the rasters on the left is shown. Scale bar, 100 μm. See also Figures S1 and S2.

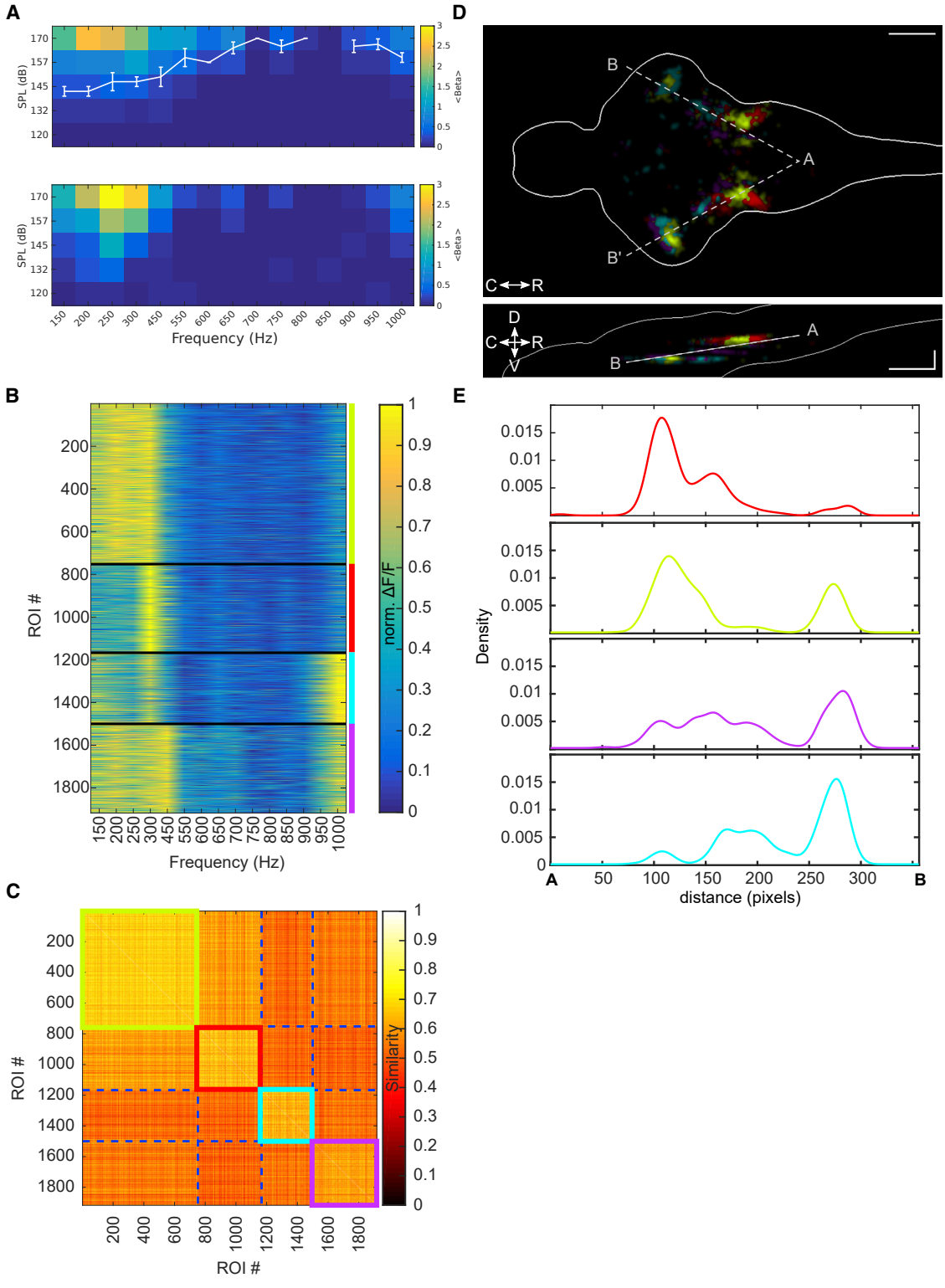

Figure 2. Spatially Distinct Clusters Represent Low- and High-Frequency Information

(A) Top: average audiogram (5 larvae at 8 dpf), measured as the amplitude of the neuronal response fit by a linear regression model, averaged over all ROIs in the brain. White curve: average threshold and SEM are shown. Bottom: single larva example is shown.

(B) Frequency tuning curves for 13 larvae at 8 dpf, grouped in 4 clusters using k-means clustering algorithm with Euclidean distance on normalized ΔF/F values. Different larvae were imaged at different optical sections. Clusters 1–4 are represented in red, green, cyan, and magenta.

(legend continued on next page)

by the emitted sound of shuffling rocks, as they probably learned to associate it with new food sources previously hidden under the rocks [35].

Frequency Representation in the Brain

To study how auditory stimuli of different frequencies are represented in the brain of the larva, we first calculated the larvae audiograms (STAR Methods). The audiograms displayed two main frequency bands: a low-frequency band from 150 to 450 Hz and a high-frequency band from 950 to 1,000 Hz. The average amplitude threshold was 138 ± 3.05 dB for the low-band frequency (Figure 2A). We then computed the frequency tuning curves of each responsive ROI across the auditory circuits of the larva. To study the tuning curves, we used auditory stimuli with an amplitude of 155 dB (an amplitude above the detectable threshold, capable of triggering motor behaviors and inducing strong, but not saturated, neuronal circuit responses; Figure 2A). Using k-means, we found that, among all ROIs, the frequency tuning curves could be classified in four main clusters that best represented the diversity of the obtained tuning curves (Figures 2B and 2C; STAR Methods). Among these clusters, two contained a frequency band ranging from 150 to 450 Hz and two others had an additional high-frequency band at 950 and 1,000 Hz. The use of 4 clusters was supported by two clustering validation methods (Silhouette and Calinski-Harabasz index; Figure S5A) and two alternative and independent clustering approaches (principal-component analysis and hierarchical clustering; Figures S5B and S5C). The stimulus-induced neuronal responses were principally auditory because ablation of the lateral line was relatively similar to those observed under normal conditions (especially in the low-frequency band; Figure S4).

To study the spatial organization of these four clusters across the different brain regions, we registered the brains' anatomy of each recorded larvae (8 dpf; n = 13) to a common reference space using an affine transformation (STAR Methods). We subsequently computed a normalized 3D density map for each cluster and projected the maximum density along the dorsoventral and mediolateral axis (Figure 2D; STAR Methods). We observed that the different clusters were organized along a rostrocaudal axis (dashed line in Figure 2E), encompassing both the octaval nucleus and the torus semicircularis. The density histogram along this axis for each cluster (STAR Methods) showed that clusters with only the low-frequency band (150 and 450 Hz) were more represented in the caudal part of the axis (the octaval nuclei), although the clusters containing the high-frequency band (950 and 1,000 Hz) were more represented in the rostral part of the axis (the torus semicircularis; Figure 2E).

This finding suggests that 8-dpf zebrafish larvae may process two relevant frequency bands via two different pathways. Low frequencies are locally processed in the hindbrain although low and high bands are transferred to the midbrain.

Development of the Auditory Responses

To find out whether the low dimensionality in the response profiles was the consequence of an immature nervous system and to study whether it changes as the larva develops, we reproduced these analyses at different developmental stages (from 7 to 21 dpf). We first observed that there were no major changes in terms of the audiograms (Figures 3A and S3A), and their detection thresholds were not significantly different across the different developmental stages (average 7 dpf, 141.8 ± 3.11; average 8 dpf, 137.5 ± 3.0; average 9 dpf, 144.9 ± 2.7; average 14 dpf, 136.6 ± 4.1; average 21 dpf, 142.5 ± 4.7; $p = 0.44$; ANOVA; Figures 3A, S3A, and S3B). Moreover, the 4 types of tuning curves across the different developmental stages were also very similar (Figure 4; average correlation: 0.85 ± 0.14; Figure 4C). The only exceptions were two clusters at 9 dpf, with tuning curves showing the emergence of a new mid-range frequency band at ~650 Hz (Figures 4A and 4B). This mid-range band was still observed at 14 dpf but fully disappeared at 21 dpf.

Auditory-Induced Motor Behaviors

To further understand the biological relevance of these two auditory processing channels, we presented to the zebrafish larvae auditory stimuli of different frequencies while monitoring their motor behavior (tail deflections) using a high-speed camera (STAR Methods).

Previous studies showed that strong acoustic or vibrational stimuli can trigger startle responses of two different types: short-latency C-start (SLC) (~5 ms) and long-latency C-start (LLC) (~28 ms) [36, 37]. SLC responses are triggered by strong auditory stimuli and are Mauthner cell dependent. In contrast, LLCs are elicited by weaker auditory stimuli and are otolith dependent [37].

To study the type of tail movements elicited by the auditory stimuli, we computed the latency from the stimulus to the onset of the induced motor behavior. For this purpose, we used two types of broad-band noise auditory stimuli: high amplitude (170 dB) and low amplitude (155 dB; the amplitude used in this study). We observed that high-amplitude stimuli generated movements with a probability of 0.92 and latencies displaying a bimodal distribution. The short latency population had an average latency of 11.82 ± 2.51 ms, most probably corresponding to SLCs. The longer latency population had an average latency of 60.62 ± 13.33 ms, resembling LLCs. In contrast, lower amplitude stimuli (155 dB) induced tail motor behaviors with a probability of 0.4 and more sparsely distributed latencies with an average of 150.75 ± 65.73 ms. The latter were significantly longer than those of LLCs ($p = 5 \times 10^{-14}$; rank-sum; Figure 5A). We named this type of behavior as long-latency tail movements (LLTMs), because they resembled symmetrical or asymmetrical scoots rather than C-start-like tail movements (Figure 5A) [38]. These results suggest that the amplitude of the auditory stimuli used throughout the experiments induces tail motor behaviors mediated by a neuronal circuit integration process rather than a rapid reflex response.

(C) Similarity matrix based on the Euclidean distance for the clusters in (B).

(D) Spatial distribution of the 4 clusters presented in (B). All 13 larvae were aligned on a reference stack using affine transformation. Top: maximum density projection across the Z axis is shown. Bottom: maximum density projection across the y axis is shown. Scale bar, 100 μm.

(E) Spatial density of ROIs for each cluster along the gray dashed AB axis in (D), averaged across both hemispheres. See also Figures S4 and S5.

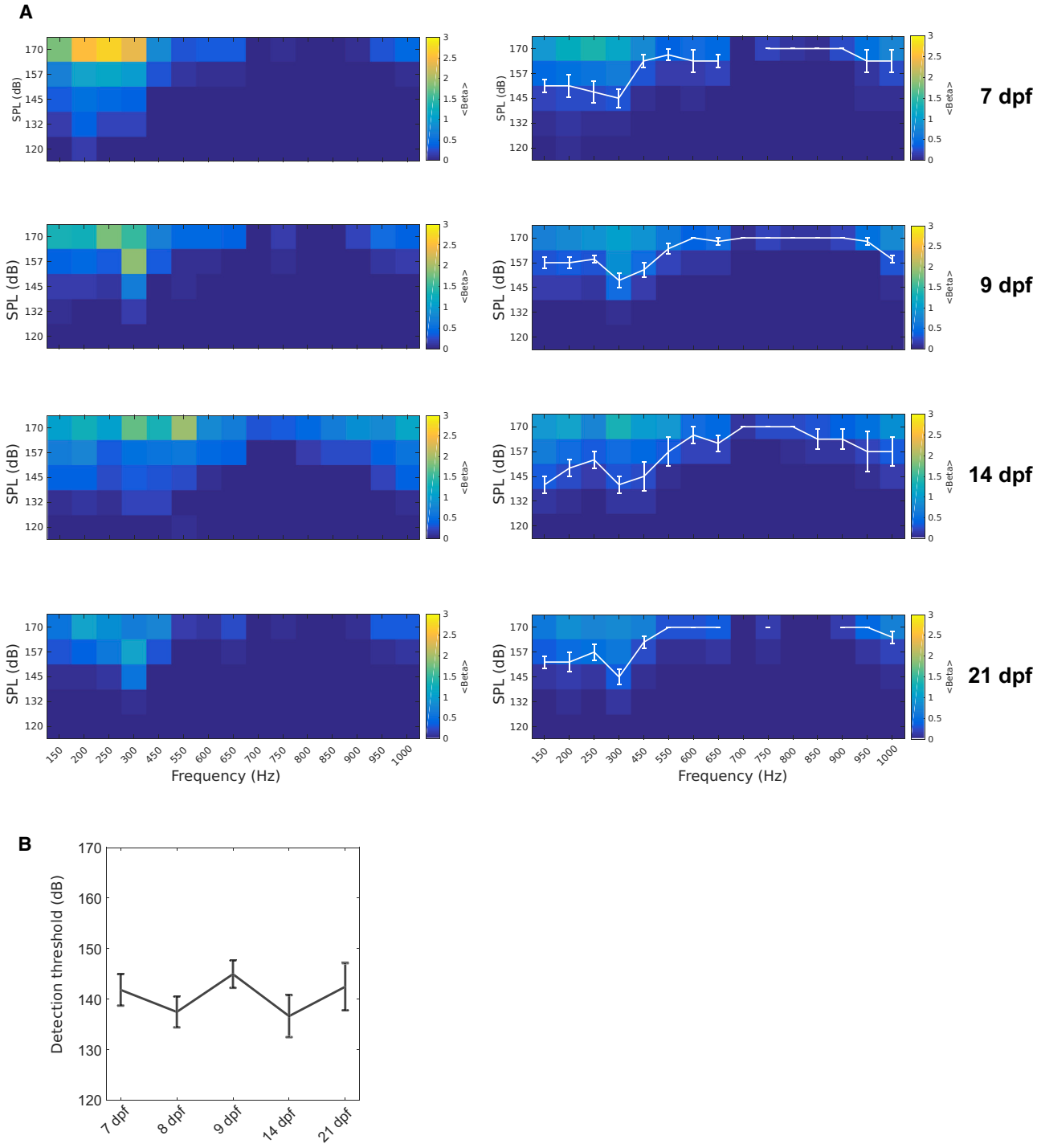

Figure 3. Audiograms at Different Development Stages

(A) Right: average audiogram at 7 dpf (4 larvae), 9 dpf (7 larvae), 14 dpf (3 larvae), and 21 dpf (5 larvae) measured as the amplitude of the neuronal response fit by a linear regression model, averaged over all ROIs in the brain. White curve: average threshold and SEM are shown. Left: single larva example is shown.

(B) Detection threshold, the lowest amplitude at which a neuronal response was detected, averaged across larvae during the different developmental stages (mean ± SEM). Means at different ages were not significantly different ($p = 0.4381$; one-way ANOVA). See also Figure S3.

To infer the significance of the correlation between auditory stimulation and LLTMs, we compared the datasets against a set of shuffled motor events. In this null model, the inter-event distribution of tail bouts was preserved but the onset of tail bouts was randomized (STAR Methods). Using this null model, we defined a threshold corresponding to the 95th percentile of its

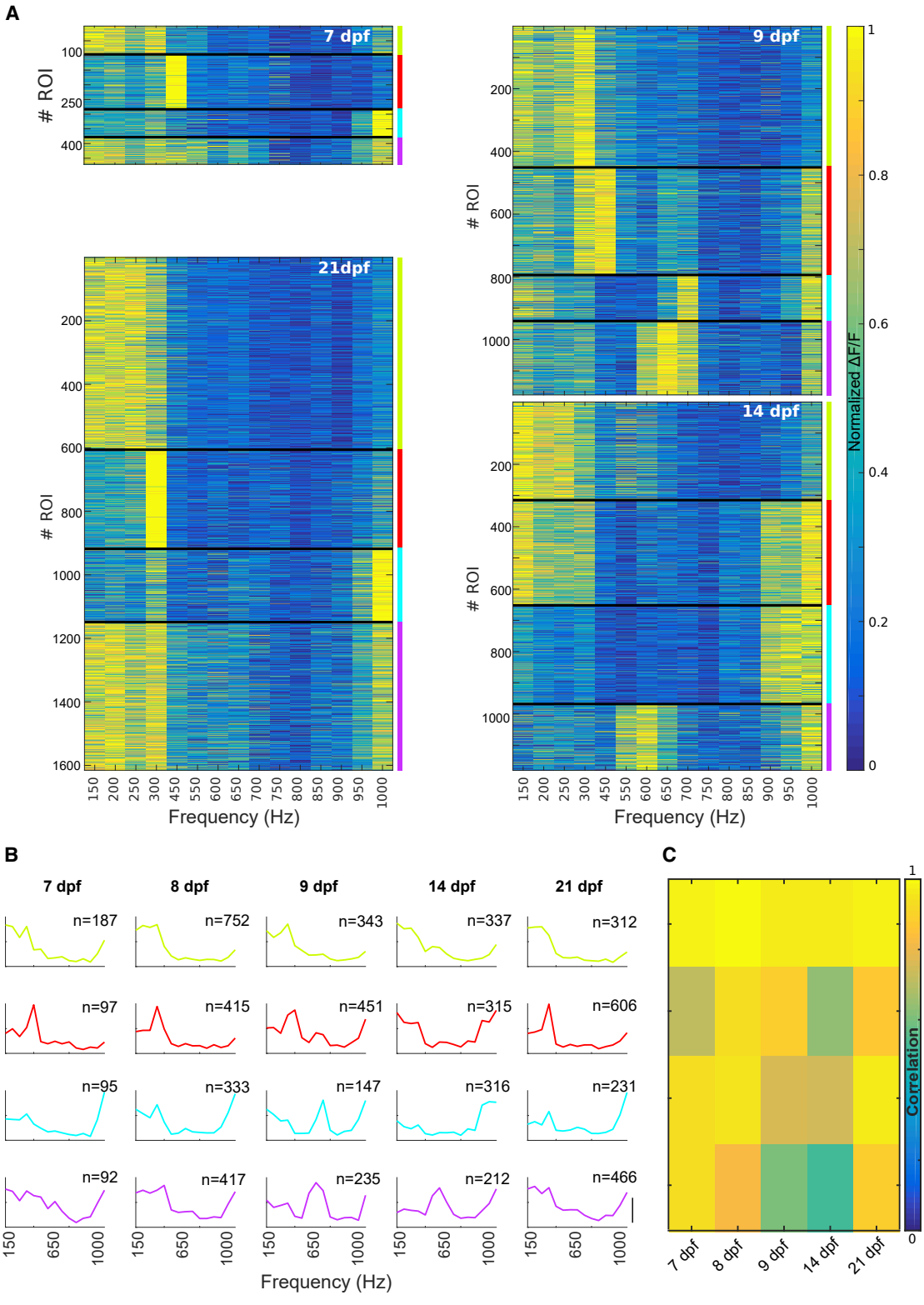

(legend on next page)

distribution that enabled us to determine whether the auditory stimuli significantly induced motor behaviors. We observed that auditory stimuli of frequencies ranging from 150 Hz to 450 Hz were able to significantly elicit tail movements ($p < 10^{-4}$ for 150–400 Hz; $p = 0.014$ for 450 Hz after Bonferroni correction). Frequencies of 150 and 300 Hz were capable of inducing a motor behavior with a probability above 0.25. Auditory stimuli of 950 Hz and 1,000 Hz also significantly induced motor behaviors ($p = 0.014$ for 950 Hz; $p = 0.041$ for 1,000 Hz after Bonferroni correction) but with a much lower probability (0.1). Furthermore, the amplitude of the auditory-induced tail movements displayed a bimodal distribution, probably reflecting two different types of movements. When we compared the distributions of tail movement amplitudes elicited by low- or high-frequency band stimuli, we observed that both distributions were not significantly different ($p = 0.73$; rank-sum; Figure 5C).

Sensorimotor Transformation

To characterize the neuronal processes mediating the auditory sensorimotor transformations, we described each ROI according to a sensorimotor ratio. For this purpose, we first computed (1) the level of correlation of the Ca^{2+} transients of each ROI with the presentation of the auditory stimulus, which we defined as the percentage of variance of the stimulus responses explained by the linear model (R^2_{stim}; Figure S2A; STAR Methods) and (2) the level of correlation of the Ca^{2+} transients of each ROI with the generation of a tail movement. For the latter, we also used a regression-based approach. Because ROIs correlated with behavior could be active before or after the onset of a movement, we used a series of regressors (one for each time frame) that spanned 3.5 s around the onset of each tail movement. The goodness of fit (R^2_{mvt}) was computed for the whole series of regressors (Figure S2D; STAR Methods).

We then defined the sensorimotor ratio (SMR) as the difference between the percentage of variance explained by the stimulus and the behavior regressors divided by the total fraction of the explained variance: $SMR = (R^2_{mvt} - R^2_{stim})/(R^2_{mvt} + R^2_{stim})$. This ratio ranges from −1 (purely sensory) to +1 (purely behavior related; Figure S6).

Using this approach, we identified (1) ROIs whose variance was mostly explained by the sensory inputs, (2) a group of ROIs whose variance was mostly explained by the occurrence of a motor behavior, and (3) a group of ROIs whose variance was explained by both stimuli and behavior (2,915 ROIs from 10 larvae; Figures 5D and 6A, left; STAR Methods). The latter may represent candidate ROIs involved in the sensorimotor transformations (Figures 6A and 6B; Video S1). This approach revealed that ROIs with a large positive sensorimotor ratio (motor ROIs) were also active during self-generated (spontaneous) behaviors (Figure 5D). This suggests that the same motor circuit rather than an auditory dedicated one is active during self-generated and auditory-evoked motor behaviors (Figure 5D). This was further confirmed at the whole population level (n = 27 larvae), where we found similar levels of activity during self-generated and auditory-induced tail movements for ROIs with large positive sensorimotor ratios (motor ROIs; Figures S7A–S7C).

To visualize the topography of the ROIs according to their sensorimotor ratio, we aligned the positions of each ROI to a reference brain (Figure 6A, right panel; STAR Methods), which was then aligned to the z-brain atlas [39]. The latter enabled the identification of anatomical regions (Figures 6D and 6E) and the neuron types (glutamatergic, GABAergic, and glycinergic; Video S2). The average sensorimotor map showed auditory sensory areas in (1) the octaval nuclei (ON), which contained anatomically segregated glutamatergic, GABAergic, and glycinergic neurons; (2) parts of the cerebellum containing two segregated groups of glutamatergic and GABAergic neurons; and (3) the torus semicircularis (mostly GABAergic). The motor ROIs were mainly observed in (4) the reticulo-spinal circuit (overlapping glutamatergic, GABAergic, and glycinergic neuronal populations), (5) the cerebellum (anatomically segregated glutamatergic and GABAergic neurons), and (6) the rostral part of the nucleus of the medial longitudinal fascicle (nucMLF), which was mainly glutamatergic. Sensorimotor regions were localized at the boundaries of the sensory areas at the intersection with the motor regions. In addition, sensorimotor circuits were also observed toward the caudal part of the nucMLF (Figures 6A, 6D, and 6E; Video S2).

To learn about the mechanisms underlying the sensorimotor transformations, we grouped our ROIs from 10 larvae into bins based on the value of their sensorimotor ratio. We pooled together results from stimulus frequencies that robustly elicited behavioral responses (150–450 Hz). We took advantage of the variability in the behavioral outcome of the auditory stimulations and averaged the activity of ROIs in each sensorimotor bin across trials for which the auditory stimuli failed to induce a behavioral response (black curve, top row, Figures 6B and 6C) and across trials where auditory stimuli elicited a tail bout (orange curve, top and bottom row, Figures 6B and 6C). We also averaged the neural activity around the onset of spontaneous movements (purple curve, bottom row, Figures 6B and 6C). The average over trials was once time locked to the onset of the stimuli (Figures 6B and 6C, top row) and once to the onset of the tail movements (Figures 6B and 6C, bottom row). We observed that ROIs with a low sensorimotor ratio (sensory ROIs) faithfully represented sensory information independently of the behavioral outcome (Figures 6B and 6C, top left). Reciprocally, ROIs with a high sensorimotor ratio (motor ROIs) represented motor-related information with similar levels of activity

Figure 4. Frequency Tuning Curves at Different Developmental Stages

(A) Frequency tuning curves grouped in 4 clusters using k-means clustering algorithm at 7 dpf (6 larvae), 9 dpf (11 larvae), 14 dpf (3 larvae), and 21 dpf (5 larvae).

(B) Average normalized tuning curves across ROIs grouped in 4 clusters throughout the larva's development, from 7 to 21 dpf. Similar tuning curves were assigned to the same cluster across developmental stages by maximizing the correlation between the tuning curves and the average tuning across ages. Scale bar, 0.5 ΔF/F. The colors represent the clusters indicated in (A). Top right corner: the number of ROIs per cluster is shown.

(C) Correlation matrix used to order the clusters in (B). We correlated the tuning curve for each cluster at each developmental stage with the average tuning curve across ages. All possible permutations of cluster assignments were tested. The matrix shows the solution that maximized the average correlation. Average correlation: 0.85 ± 0.14 (SD).

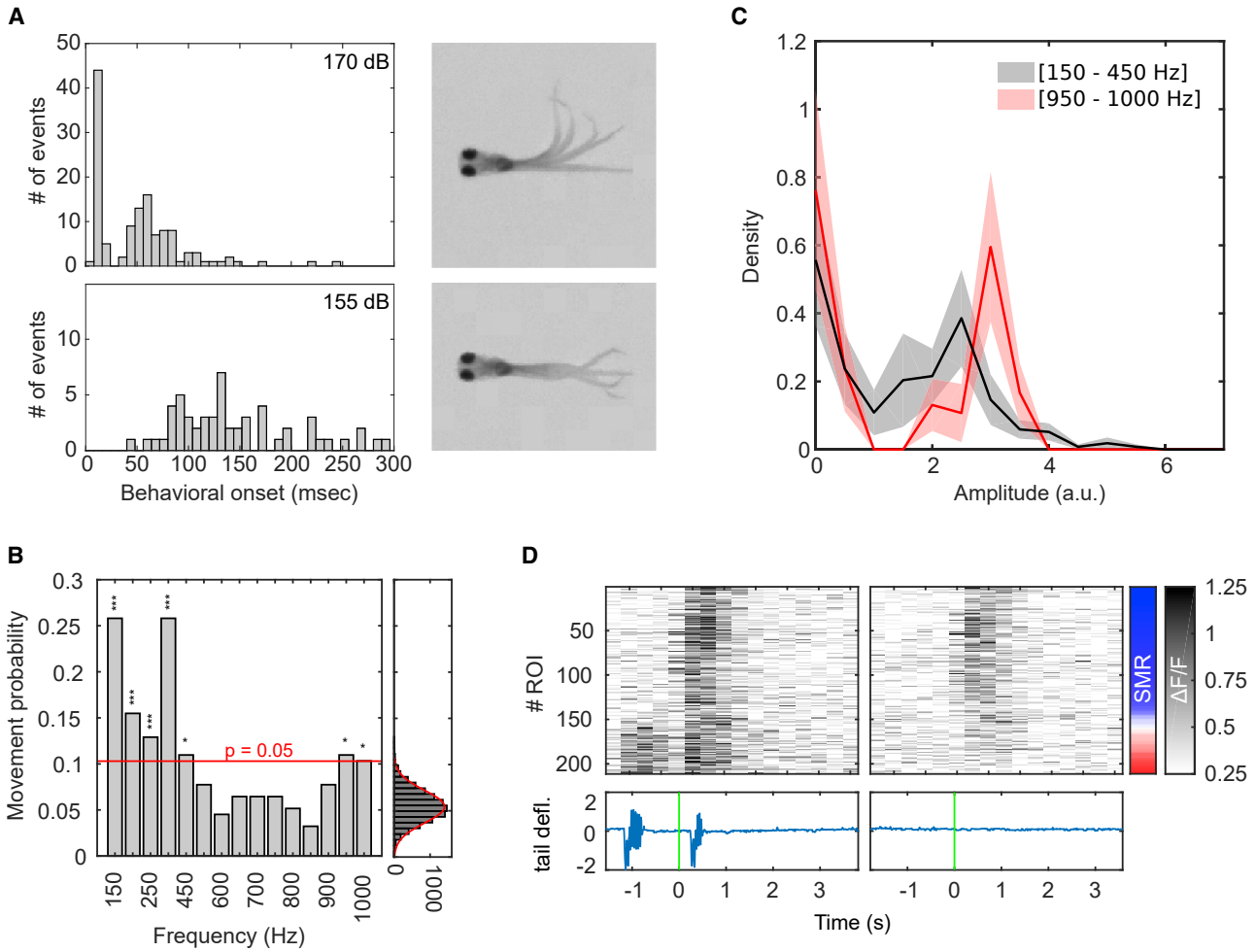

Figure 5. Auditory-Induced Tail Motor Behaviors

(A) Delay histogram between the onset of auditory stimulation and the onset of tail movements (7 larvae) Top: auditory stimulation using 170 dB re 1 μPa stimuli resulted in a bimodal distribution probably representing short latency C-starts and long-latency C-starts. Bottom: auditory stimulation using 155 dB re 1 μPa stimuli resulted in a distribution of longer and more variable latencies.

(B) Probability of having at least one tail bout in a 500-ms time window after stimulus onset for each frequency. A null model was created by generating data following the same inter-bouts interval distribution as the experimental data (left). p values were computed using the null model distribution and subsequently adjusted using Bonferroni correction. Red dashed line, significance threshold for $\alpha = 0.05$ after Bonferroni correction. n = 10 larvae.

(C) Average density distribution (mean ± SEM) of bout amplitudes (10 larvae), elicited by low-frequency stimuli (150 Hz and 450 Hz; 134 bouts) in black and high-frequency stimuli (950 Hz and 1,000 Hz; 30 bouts) in red. The amplitude of a tail bout was defined as the maximum curvature during the bout. The medians of the two distributions were not significantly different (p = 0.73; two-sided rank-sum test).

(D) Top: single trial raster on a single larva. ROIs are ordered by their sensorimotor ratio, computed as $(R^2_{mvt} - R^2_{stim})/(R^2_{mvt} + R^2_{stim})$. The sensorimotor ratio ranges from −1 (sensory ROIs, in blue) to +1 (behavior-related ROIs, in red). Bottom: tail deflection is shown, green bar, auditory stimulus onset.

independently of the sensory stimuli (Figures 6B and 6C, bottom right). In contrast, ROIs with a sensorimotor ratio close to zero (sensorimotor ROIs) showed levels of activity that were significantly different when a stimulus induced a motor behavior than when the stimulus failed to induce one (Figures 6B and 6C).

To further study of the temporal dynamics of the auditory sensorimotor transformations, we used light-sheet microscopy using high-acquisition rates (20 Hz). We recorded the neural activity and the motor behavior of 27 larvae in response to a broadband auditory stimulus (250–1,000 Hz; Figure 7A; Video S2; STAR Methods). Using this approach, we calculated the onset of the calcium transients with respect to the onset of the auditory stimuli (STAR Methods; Figure 7A). We observed that neuronal responses to auditory stimuli that failed to trigger a motor behavior were limited to the sensory ROIs (Figure 7B). In contrast, sensory stimuli that successfully triggered a motor behavior induced neuronal responses among ROIs with a full spectrum of sensorimotor ratios (Figure 7B). This analysis and the spatial distribution of the onsets of the different ROIs (Figure 7D) suggest that information flows from sensory to motor-related areas via the sensorimotor ROIs. The latter is also supported by the positive correlation between the averaged onset of the ROIs against the sensorimotor ratio (Figure 7C).

To investigate the mechanisms mediating the sensorimotor transformations in the zebrafish auditory system, we calculated (1) the number of activated ROIs (ROIs whose activity was above

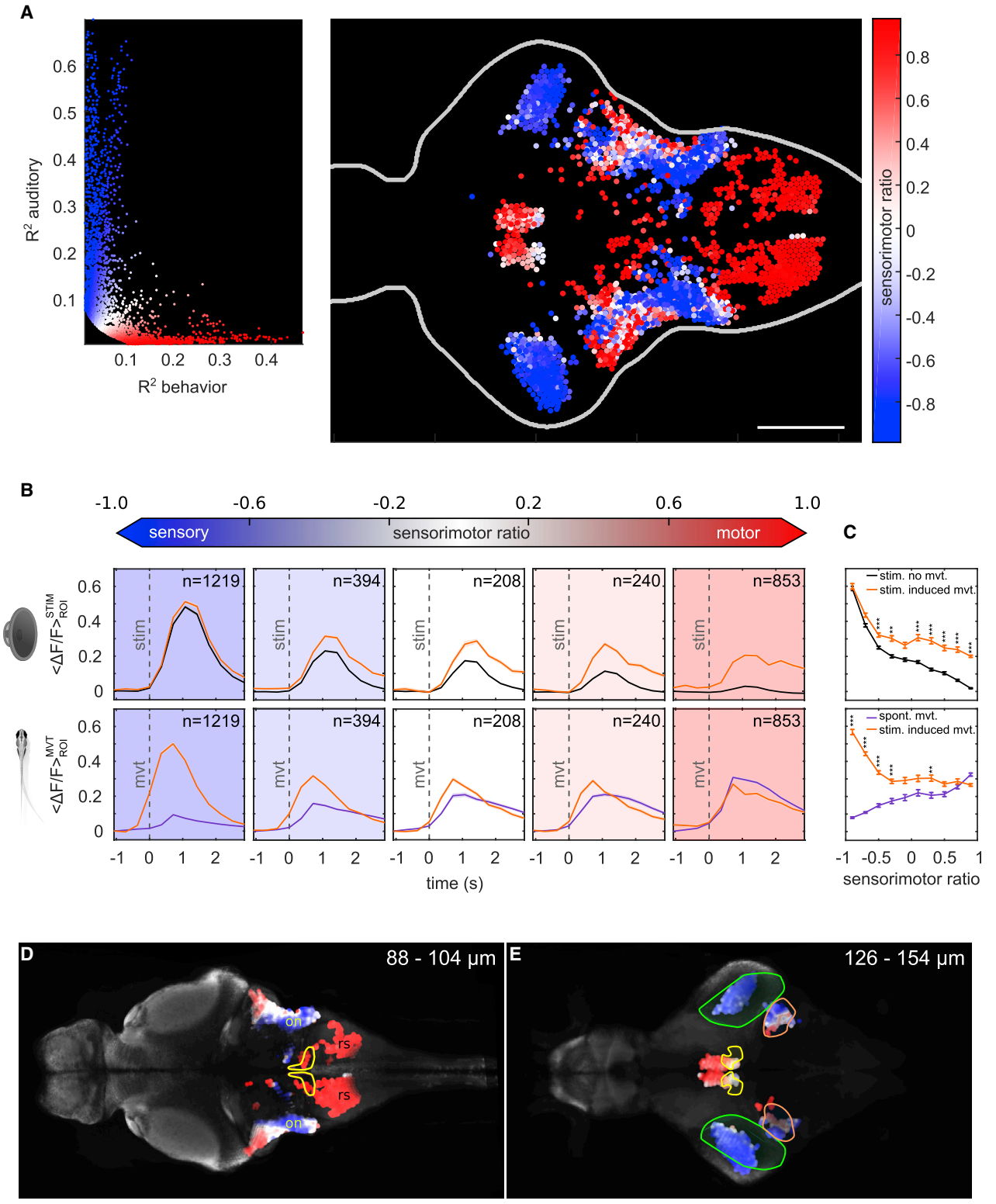

Figure 6. Sensorimotor Properties of the Auditory Neural Circuit

(A) Left: distribution of ROIs R^2 values for movement and behavior with the corresponding sensorimotor ratio value. Right: topography of ROI's sensorimotor ratio for 10 larvae at 8 dpf is shown. Scale bar, 100 µm.

(B) Top: average ΔF/F over ROIs after an auditory stimulation around auditory stimulus onset (t = 0 s) for ROIs grouped in 5 bins according to their sensorimotor ratio. Stimulus frequencies from 150 to 450 Hz were pooled together. Orange curve, stimulus followed by a tail movement within a 500-ms time window after

(legend continued on next page)

a threshold of 2 SDs from the average activity, 500 ms before stimulation), (2) the ΔF/F, and (3) the duration of the auditory-induced Ca^{2+} transients for the ROIs of different sensorimotor ratios, when the stimulus induced a motor behavior or when it failed to do so (Figure 7E). We observed that the number of recruited ROIs with low sensorimotor ratios (sensory ROIs) when stimuli induced a motor behavior was not significantly different from the number of recruited ROIs than for trials in which the stimuli failed to do so (Figure 7E, top; p = 0.1936, 0.0323, 0.0059, 0.0024, and 0.0003; one-tailed paired Wilcoxon signed-rank test after Bonferroni correction). Along the same lines, the ΔF/F of the induced Ca^{2+} transients in sensory ROIs when the stimuli succeeded in inducing a motor behavior was not significantly different from the ΔF/F than for trials in which stimuli failed to do so (Figure 7E, middle). However, for the sensorimotor ROIs, the amplitude of the induced Ca^{2+} events was significantly higher when a stimulus induced a tail movement than when it did not (Figure 7E, middle; p = 1, 0.0096, 0.0011, 0.0015, and 0.0391; one-tailed paired Wilcoxon signed-rank test after Bonferroni correction). In contrast, the duration of the induced Ca^{2+} transients was significantly larger for the sensory and sensorimotor ROIs when a tail movement followed the auditory stimulation (Figure 7E, bottom; p = 0.0162, 0.0131, 0.0052, 0.0037, and 0.7812; one-tailed paired Wilcoxon signed-rank test after Bonferroni correction). These results show that the duration of the auditory-induced response is determinant for the sensorimotor transformations. In addition, we observed that ongoing spontaneous activity before the onset of the auditory stimulation failed to predict the outcome of the sensory response (Figure S7D). Thus, we suggest that the increase in duration of the auditory responses does not result from its integration with the current state of the network, but it rather represents the integration of the sensory response in order to activate the sensorimotor and motor circuits.

DISCUSSION

The neuronal representation of sensory information has been exhaustively studied. However, how this information is then integrated and transformed into motor patterns still remains elusive. In this study, we simultaneously recorded auditory-induced neuronal responses of both sensory and motor circuits while monitoring tail motor movements. We found auditory-induced responses to frequencies ranging from 150 to 1,000 Hz in the octaval nuclei, the torus semicircularis, the eminentia granularis, and the nucleus of the lateral longitudinal fascicle [40].

The audiograms of zebrafish larva displayed sensitivities for two main frequency bands (150–450 Hz and 950–1,000 Hz), as observed in [11].

In contrast to other studies that suggest a tonotopic organization in fish [13, 14, 41], here, we only found four different frequency response profiles represented in the brain. These four different types of tuning curves involved low- and high-frequency bands. These two bands may directly emerge from the mechanical properties of the two different populations of the saccular hair cells (rostral saccular afferents respond to high frequencies although caudal afferents are tuned to lower frequencies) [11], probably due to mechanical properties of the hair cells [42].This low-dimensional auditory representation of sound frequency in the zebrafish larvae is different from the high-dimensional processing in cochlear animals where neurons with sharp and broader tuning curves are observed for a large range of frequencies across several auditory brain regions [11], along with many other neurons with more complex response profiles: sound onsets and offsets of particular amplitude; amplitude modulation; frequency modulation; or harmonicity [43], for which more complex methods are necessary for their response description (e.g., spectro-temporal receptive fields) [44].

Two of these profiles were sensitive to low-frequency bands, which were processed locally in the hindbrain. The two others were bimodal, containing a low-frequency band and an additional high-frequency one. They were both represented in the hindbrain and the midbrain of the larva. This finding suggests that young larvae may process low and high frequencies differently via two different channels with different biological or functional relevance. Low frequencies are locally processed in the hindbrain to generate motor behaviors (e.g., the largemouth predator generates ~200 Hz when attacking prey) [34], although low and high bands are transferred to the midbrain. It is possible that the latter channel serves for modulation of the tectal visual response because previous studies showed that simultaneous presentation of visual and auditory stimuli to zebrafish larva reduced the visual response in the optic tectum [30]. This hypothesis is supported by the fact that tail movements were induced mainly by low-frequency sounds and that the auditory responses in the torus semicircularis were colocalized with mainly GABAergic neurons.

Both audiograms and tuning curves did not differ much between 7 and 21 dpf. The audiograms and the auditory thresholds at the different developmental stages were relatively similar. The 4 types of frequency tuning curves were also observed at all developmental larval stages. Therefore, we suggest that the low-dimensional encoding in zebrafish larvae emerges early in development and remains stable thereafter. However, a mid-range-frequency band transiently emerged at 9 dpf, disappearing around 21 dpf. Whether this transient frequency band

stimulus onset. Black curve, stimulus not followed by a tail movement. Bottom: average ΔF/F across ROIs when the fish moved is shown (t = 0 s: movement onset). Orange curve, tail movement preceded by an auditory stimulation. Purple curve, self-generated movement. In the bottom panels, the delay between the orange curve (stimulus-induced movement) and the purple curve (self-generated movement) corresponds to sensory processing, because the stimulus occurs before the movements.

(C) Average peak ΔF/F value (mean ± SEM) across ROIs around auditory stimulus onset (top panel) or tail movement onset (bottom panel). ROIs were binned into 10 groups based on their sensorimotor ratio value. Bins were compared using the two-tailed Wilcoxon rank sum test, and p values were subsequently adjusted using Bonferroni correction.

(D) The topography of the sensorimotor ratio (blue, sensory; white, sensorimotor; red, motor), superimposed to the Elavl3-GCaMP5 line in the z-brain atlas. Yellow, facial motor and octavolateralis efferent; on, octaval nuclei; rs, reticulospinal circuits. Top right corner: depth of the imaged plane is shown.

(E) The topography of the sensorimotor ratio over the Elavl3-GCaMP5 line in the z-brain atlas. Green, torus semicircularis; yellow, nucleus of the medial longitudinal fascicle; orange, cerebellar vglut2-enriched area. Top right corner: depth of the imaged plane is shown. See also Figure S6 and Videos S1 and S2.

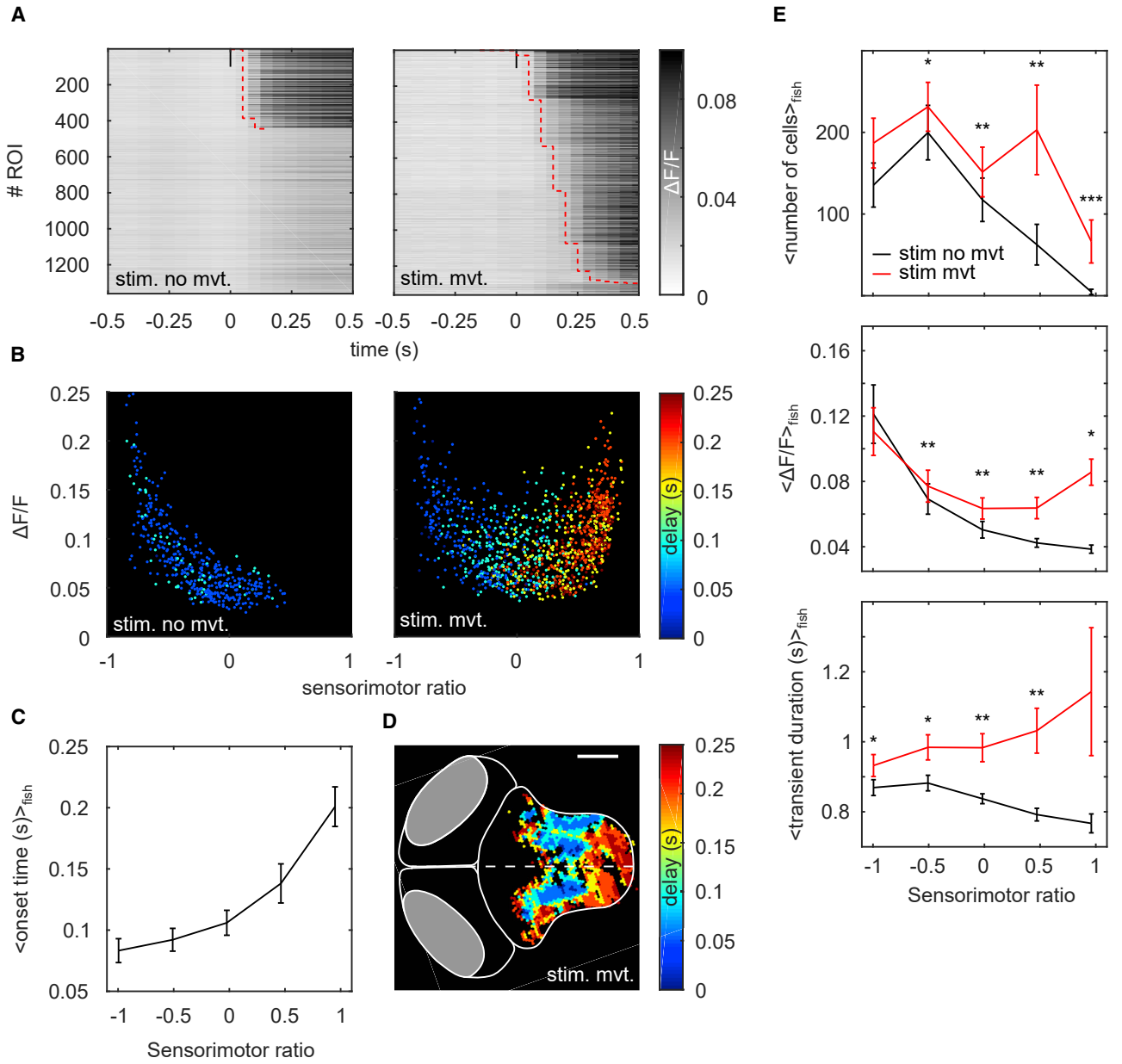

Figure 7. Increased Network Activity and Duration of Calcium Transients Mediates Sensorimotor Transformation

(A) Example rasters of a single larva averaged over trials for which auditory stimuli induced (stim. mvt.) or did not induce a tail movement (stim. no mvt.). ROIs are sorted by the onset time of their calcium transients. Red dotted line, transient onset. Transient onset was estimated only for ROIs whose activity after stimulation was 2 SDs above their mean activity before stimulation (activity baseline).

(B) Example of ΔF/F as a function of sensorimotor ratio; colormap, onset time of the calcium transients.

(C) Onset time (mean ± SEM) as a function of sensorimotor ratio for 27 larvae. ROIs were binned into 5 groups based on their sensorimotor ratio.

(D) Topography of the onset time for the same larva as in (A) and (B). Scale bar, 100 μm.

(E) Top: number of ROIs above the 3 SD threshold for each sensorimotor ratio bin (mean ± SEM). Middle: peak ΔF/F for each bin is shown (mean ± SEM). Bottom: transient duration computed as the full width at half maximum of the calcium transients for each bin is shown (mean ± SEM). Red line, auditory stimulation followed by a tail movement in a 500-ms time window after stimulation onset. Black line, auditory stimulation not followed by a tail movement. Results were pooled across 27 larvae. Bins were compared using the one-tailed Wilcoxon paired signed rank test, and p values were subsequently adjusted using Bonferroni correction. See also Figure S7.

represents a relevant developmental process remains to be determined.

The ability to simultaneously monitor neuronal activity and tail motor behavior allowed us to study the processes underlying sensorimotor transformations in the hindbrain of the larva. Using a linear regression approach to classify ROIs according to a sensorimotor ratio, we found a topographic and functional continuum of the sensorimotor representation, suggesting a gradual

transformation of sensory information into motor patterns. This continuous gradual transformation of the sensory information into motor patterns and the increase in the duration of the auditory-induced calcium transients when a stimulus induced a motor behavior suggest that the sensorimotor transformations do not reflect a gating mechanism (e.g., controlling the passage of neuronal activity from the sensory to the motor circuits by an independent modulatory circuit) [45] but rather the capacity of the circuit to integrate the auditory-induced neuronal response. This hypothesis is also supported by the long and variable latency of the induced tail movements. This increase in the duration of the calcium transients could be driven through recurrent connectivity to sufficiently amplify neural activity and reach the threshold required to activate the motor circuits.

This mechanism may help integrate auditory information to obtain reliable information about the detected stimulus to generate a relevant behavioral response.

STAR★METHODS

Detailed methods are provided in the online version of this paper and include the following:

- KEY RESOURCES TABLE
- LEAD CONTACT AND MATERIALS AVAILABILITY
- EXPERIMENTAL MODEL AND SUBJECT DETAILS
- METHOD DETAILS
  - Auditory stimulation
  - Calcium imaging
  - Data analysis
- QUANTIFICATION AND STATISTICAL ANALYSIS
- DATA AND CODE AVAILABILITY

SUPPLEMENTAL INFORMATION

Supplemental Information can be found online at https://doi.org/10.1016/j.cub.2019.10.020.

ACKNOWLEDGMENTS

We thank V. Candat and F. Bouallague for help with zebrafish, A. Kulkarni for discussions on data analysis, and O. Lahrach and Anahid Jeant-Maloumian for preliminary experiments. M.P. was supported by the Fondation pour la Recherche Medicale (FRM: FDT201904008327) and the ENS Lyon. A.J. was supported by the Fondation pour la Recherche Medicale (FRM: FDT20140930915) and the ENS Cachan. A.D. was supported by the ENS Cachan, and G.S. was supported by ERC StG 243106, ERC CoG 726280, ANR-10-LABX-54 MEMO LIFE, and ANR-11-IDEX-0001-02 PSL Research University. D.S. was supported by the Ecole Normale Supérieure invited professor program and NIH R15EY027112.

AUTHOR CONTRIBUTIONS

G.S. and M.P. designed and conducted the experiments. S.A.R., T.P., A.D., N.E., and D.S. performed preliminary experiments. M.P. analyzed the data. M.P., D.S., and G.S. wrote the manuscript. S.A.R., J.B.-W., A.J., and T.P. provided help for the data analysis and experimental design.

DECLARATION OF INTERESTS

The authors declare no competing interests.

Received: June 19, 2019
Revised: September 27, 2019
Accepted: October 15, 2019
Published: November 7, 2019

REFERENCES

1. Mann, Z.F., and Kelley, M.W. (2011). Development of tonotopy in the auditory periphery. Hear. Res. *276*, 2–15.
2. Zaretsky, M.D., and Konishi, M. (1976). Tonotopic organization in the avian telencephalon. Brain Res. *111*, 167–171.
3. Romani, G.L., Williamson, S.J., and Kaufman, L. (1982). Tonotopic organization of the human auditory cortex. Science *216*, 1339–1340.
4. Merzenich, M.M., and Schreiner, C.E. (1992). Mammalian auditory cortex—some comparative observations. In The Evolutionary Biology of Hearing, D.B. Webster, A.N. Popper, and R.R. Fay, eds. (Springer New York), pp. 673–688.
5. Carr, C.E. (1992). Evolution of the central auditory system in reptiles and birds. In The Evolutionary Biology of Hearing, D.B. Webster, A.N. Popper, and R.R. Fay, eds. (Springer New York), pp. 511–543.
6. Inoue, M., Tanimoto, M., and Oda, Y. (2013). The role of ear stone size in hair cell acoustic sensory transduction. Sci. Rep. *3*, 2114.
7. Lechner, W., Heiss, E., Schwaha, T., Glösmann, M., and Ladich, F. (2011). Ontogenetic development of weberian ossicles and hearing abilities in the African bullhead catfish. PLoS ONE *6*, e18511.
8. Higgs, D.M., Souza, M.J., Wilkins, H.R., Presson, J.C., and Popper, A.N. (2002). Age- and size-related changes in the inner ear and hearing ability of the adult zebrafish (Danio rerio). J. Assoc. Res. Otolaryngol. *3*, 174–184.
9. Popper, A.N., and Fay, R.R. (2011). Rethinking sound detection by fishes. Hear. Res. *273*, 25–36.
10. Mohr, R.A., Chang, Y., Bhandiwad, A.A., Forlano, P.M., and Sisneros, J.A. (2018). Brain activation patterns in response to conspecific and heterospecific social acoustic signals in female plainfin midshipman fish, Porichthys notatus. Brain Behav. Evol. *91*, 31–44.
11. Furukawa, T., and Ishii, Y. (1967). Neurophysiological studies on hearing in goldfish. J. Neurophysiol. *30*, 1377–1403.
12. McCormick, C.A. (1999). Anatomy of the central auditory pathways of fish and amphibians. In Comparative Hearing: Fish and Amphibians, R.R. Fay, and A.N. Popper, eds. (Springer), pp. 155–217.
13. Echteler, S.M. (1985). Tonotopic organization in the midbrain of a teleost fish. Brain Res. *338*, 387–391.
14. Vanwalleghem, G., Heap, L.A., and Scott, E.K. (2017). A profile of auditory-responsive neurons in the larval zebrafish brain. J. Comp. Neurol. *525*, 3031–3043.
15. Olive, R. (2015). Perception des écoulements et des vibrations chez la larve de poisson-zèbre: étude comportementale et imagerie. PhD thesis (Université Pierre et Marie Curie).
16. Schulze, A., Gomez-Marin, A., Rajendran, V.G., Lott, G., Musy, M., Ahammad, P., Deogade, A., Sharpe, J., Riedl, J., Jarriault, D., et al. (2015). Dynamical feature extraction at the sensory periphery guides chemotaxis. eLife *4*, e06694.
17. Tastekin, I., Khandelwal, A., Tadres, D., Fessner, N.D., Truman, J.W., Zlatic, M., Cardona, A., and Louis, M. (2018). Sensorimotor pathway controlling stopping behavior during chemotaxis in the *Drosophila melanogaster* larva. eLife *7*, e38740.
18. Álvarez-Salvado, E., Licata, A.M., Connor, E.G., McHugh, M.K., King, B.M., Stavropoulos, N., Victor, J.D., Crimaldi, J.P., and Nagel, K.I. (2018). Elementary sensory-motor transformations underlying olfactory navigation in walking fruit-flies. eLife *7*, e37815.
19. Min, S., Ai, M., Shin, S.A., and Suh, G.S.B. (2013). Dedicated olfactory neurons mediating attraction behavior to ammonia and amines in Drosophila. Proc. Natl. Acad. Sci. USA *110*, E1321–E1329.

20. Liu, H., Yang, W., Wu, T., Duan, F., Soucy, E., Jin, X., and Zhang, Y. (2018). Cholinergic sensorimotor integration regulates olfactory steering. Neuron *97*, 390–405.e3.
21. Samuel, A.D.T., and Sengupta, P. (2005). Sensorimotor integration: locating locomotion in neural circuits. Curr. Biol. *15*, R341–R343.
22. Ferezou, I., Haiss, F., Gentet, L.J., Aronoff, R., Weber, B., and Petersen, C.C.H. (2007). Spatiotemporal dynamics of cortical sensorimotor integration in behaving mice. Neuron *56*, 907–923.
23. Proville, R.D., Spolidoro, M., Guyon, N., Dugué, G.P., Selimi, F., Isope, P., Popa, D., and Léna, C. (2014). Cerebellum involvement in cortical sensorimotor circuits for the control of voluntary movements. Nat. Neurosci. *17*, 1233–1239.
24. Campagner, D., Evans, M.H., Bale, M.R., Erskine, A., and Petersen, R.S. (2016). Prediction of primary somatosensory neuron activity during active tactile exploration. eLife *5*, e10696.
25. Crochet, S., Lee, S.-H., and Petersen, C.C.H. (2019). Neural circuits for goal-directed sensorimotor transformations. Trends Neurosci. *42*, 66–77.
26. Naumann, E.A., Fitzgerald, J.E., Dunn, T.W., Rihel, J., Sompolinsky, H., and Engert, F. (2016). From whole-brain data to functional circuit models: the zebrafish optomotor response. Cell *167*, 947–960.e20.
27. Wolf, S., Dubreuil, A.M., Bertoni, T., Böhm, U.L., Bormuth, V., Candelier, R., Karpenko, S., Hildebrand, D.G.C., Bianco, I.H., Monasson, R., and Debrégeas, G. (2017). Sensorimotor computation underlying phototaxis in zebrafish. Nat. Commun. *8*, 651.
28. Chen, X., Mu, Y., Hu, Y., Kuan, A.T., Nikitchenko, M., Randlett, O., Chen, A.B., Gavornik, J.P., Sompolinsky, H., Engert, F., and Ahrens, M.B. (2018). Brain-wide organization of neuronal activity and convergent sensorimotor transformations in larval zebrafish. Neuron *100*, 876–890.e5.
29. Haesemeyer, M., Robson, D.N., Li, J.M., Schier, A.F., and Engert, F. (2018). A brain-wide circuit model of heat-evoked swimming behavior in larval zebrafish. Neuron *98*, 817–831.e6.
30. Thompson, A.W., Vanwalleghem, G.C., Heap, L.A., and Scott, E.K. (2016). Functional Profiles of Visual-, Auditory-, and Water Flow-Responsive Neurons in the Zebrafish Tectum. Curr. Biol. *26*, 743–754.
31. Bhandiwad, A.A., Zeddies, D.G., Raible, D.W., Rubel, E.W., and Sisneros, J.A. (2013). Auditory sensitivity of larval zebrafish (*Danio rerio*) measured using a behavioral prepulse inhibition assay. J. Exp. Biol. *216*, 3504–3513.
32. Zeddies, D.G., and Fay, R.R. (2005). Development of the acoustically evoked behavioral response in zebrafish to pure tones. J. Exp. Biol. *208*, 1363–1372.
33. Yao, Q., DeSmidt, A.A., Tekin, M., Liu, X., and Lu, Z. (2016). Hearing assessment in zebrafish during the first week postfertilization. Zebrafish *13*, 79–86.
34. Canfield, J.G., and Rose, G.J. (1996). Hierarchical sensory guidance of mauthner-mediated escape responses in goldfish (*Carassius auratus*) and cichlids (*Haplochromis burtoni*). Brain Behav. Evol. *48*, 137–156.
35. Holt, D.E., and Johnston, C.E. (2011). Can you hear the dinner bell? Response of cyprinid fishes to environmental acoustic cues. Anim. Behav. *82*, 529–534.
36. Burgess, H.A., and Granato, M. (2007). Sensorimotor gating in larval zebrafish. J. Neurosci. *27*, 4984–4994.
37. Jain, R.A., Wolman, M.A., Marsden, K.C., Nelson, J.C., Shoenhard, H., Echeverry, F.A., Szi, C., Bell, H., Skinner, J., Cobbs, E.N., et al. (2018). A forward genetic screen in zebrafish identifies the G-protein-coupled receptor CaSR as a modulator of sensorimotor decision making. Curr. Biol. *28*, 1357–1369.e5.
38. Jouary, A., and Sumbre, G. (2016). Automatic classification of behavior in zebrafish larvae. bioRxiv. https://doi.org/10.1101/052324.
39. Randlett, O., Wee, C.L., Naumann, E.A., Nnaemeka, O., Schoppik, D., Fitzgerald, J.E., Portugues, R., Lacoste, A.M.B., Riegler, C., Engert, F., and Schier, A.F. (2015). Whole-brain activity mapping onto a zebrafish brain atlas. Nat. Methods *12*, 1039–1046.
40. Fay, R.R., and Edds-Walton, P.L. (2008). Structures and functions of the auditory nervous system of fishes. In Fish Bioacoustics, J.F. Webb, R.R. Fay, and A.N. Popper, eds. (Springer New York), pp. 49–97.
41. Smith, M.E., Schuck, J.B., Gilley, R.R., and Rogers, B.D. (2011). Structural and functional effects of acoustic exposure in goldfish: evidence for tonotopy in the teleost saccule. BMC Neurosci. *12*, 19.
42. Lanford, P.J., Platt, C., and Popper, A.N. (2000). Structure and function in the saccule of the goldfish (Carassius auratus): a model of diversity in the non-amniote ear. Hear. Res. *143*, 1–13.
43. Kuchibhotla, K., and Bathellier, B. (2018). Neural encoding of sensory and behavioral complexity in the auditory cortex. Curr. Opin. Neurobiol. *52*, 65–71.
44. Klein, D.J., Depireux, D.A., Simon, J.Z., and Shamma, S.A. (2000). Robust spectrotemporal reverse correlation for the auditory system: optimizing stimulus design. J. Comput. Neurosci. *9*, 85–111.
45. Mu, Y., Li, X.Q., Zhang, B., and Du, J.L. (2012). Visual input modulates audiomotor function via hypothalamic dopaminergic neurons through a cooperative mechanism. Neuron *75*, 688–699.
46. Boulanger-Weill, J., Candat, V., Jouary, A., Romano, S.A., Pérez-Schuster, V., and Sumbre, G. (2017). Functional interactions between newborn and mature neurons leading to integration into established neuronal circuits. Curr. Biol. *27*, 1707–1720.e5.
47. Pologruto, T.A., Sabatini, B.L., and Svoboda, K. (2003). ScanImage: flexible software for operating laser scanning microscopes. Biomed. Eng. Online *2*, 13.
48. Harris, J.A., Cheng, A.G., Cunningham, L.L., MacDonald, G., Raible, D.W., and Rubel, E.W. (2003). Neomycin-induced hair cell death and rapid regeneration in the lateral line of zebrafish (Danio rerio). J. Assoc. Res. Otolaryngol. *4*, 219–234.
49. Rohlfing, T., and Maurer, C.R., Jr. (2003). Nonrigid image registration in shared-memory multiprocessor environments with application to brains, breasts, and bees. IEEE Trans. Inf. Technol. Biomed. *7*, 16–25.

STAR★METHODS

KEY RESOURCES TABLE

REAGENT or RESOURCE	SOURCE	IDENTIFIER
Chemicals, Peptides, and Recombinant Proteins		
Neomycin sulfate	Sigma-Aldrich	CAS: 1405-10-3
Experimental Models: Organisms/Strains		
Zebrafish: Tg(huC:GCaMP5G)^{ens102Tg}	[46]	RRID: ZDB-ALT-161209-7
Software and Algorithms		
MATLAB 2016a	Mathworks	https://www.mathworks.com/
ScanImage 3.8 (Calcium recordings acquisition)	[47]	http://scanimage.vidriotechnologies.com
HCImageLive 4.3 (Image acquisition)	Hamamatsu	https://hcimage.com/hcimage-overview/hcimage-live/

LEAD CONTACT AND MATERIALS AVAILABILITY

This study did not generate new unique reagents. Further information and requests for resources and reagents should be directed to Lead Contact, Germán Sumbre (sumbre@biologie.ens.fr).

EXPERIMENTAL MODEL AND SUBJECT DETAILS

Experiments were performed on transgenic zebrafish larvae from 7 to 21 dpf, expressing pan-neuronally the genetically encoded calcium indicator GCaMP5 (*Huc:GcaMP5* nacre line). The embryos were collected and raised at 28 °C in 0.5x E3 embryo medium. Larvae were kept under 14/10 hours on/off light cycles and fed after 5 dpf with Paramecia. All experiments were approved by the Comité d'éthique pour l'expérimentation animale Charles Darwin (03839.03).

METHOD DETAILS

Auditory stimulation

Stimulation protocol

We designed and 3D printed two recording chambers (one for the two-photon microscope and one for the light-sheet microscope) to deliver auditory stimuli via waterproof speakers (*Visaton K28 WP*) while simultaneously recording neural activity and motor behavior (Figure 1A). We designed two stimulation protocols:

(1) To study stimulus frequency representation: we delivered pure tones of 15 different frequencies (150, 200, 250, 300, 450, 550, 600, 650, 700, 750, 800, 850, 900, 950 and 1000 Hz). These frequencies were randomly presented for 1 s with inter-stimulus intervals of 10 s. Each frequency was presented 5 times for each experiment. To minimize the generation of unwanted harmonics, the stimuli were cosine-squared gated with a raise and decay time of 150 ms. To overcome the non-linearities of the speakers and the complex acoustic properties of the chamber, we used a miniature hydrophone (*Bruel and Kjaer 8103*) and a triaxial accelerometer (*PCB Piezotronics W356A12*) to equalize the amplitude and the acceleration of the emitted stimuli. Both probes were placed inside the chamber, 2 cm away from the speaker (Figure S1).

(2) To study sensorimotor transformations: we monitor Ca^{2+} dynamics using a light-sheet microscope with a high acquisition rate (20 Hz). Due to the constraints of the light-sheet microscope, the recording chamber was relatively small (45 × 36 × 33 mm), making impossible to record sound pressure levels. Therefore, we presented only one broadband auditory stimulus (between 250 and 1000 Hz). This stimulus was presented for 500 ms and were separated by an inter-stimulus interval of 30 s. The stimulus was repeated 55 times.

Audiograms

In order to assess the hearing thresholds of larvae, we delivered acoustic stimuli at 5 different intensity levels while recording neural activity. We delivered pure tones of 15 different frequencies (150, 200, 250, 300, 450, 550, 600, 650, 700, 750, 800, 850, 900, 950 and 1000 Hz). We calibrated the recording chamber using a miniature hydrophone (*Bruel and Kjaer 8103*) and a triaxial accelerometer (*PCB Piezotronics W356A12*) to equalize the amplitude and the acceleration of the emitted stimuli. The 5 sound pressure levels and corresponding particle acceleration levels were set to 120, 132, 145, 157 and 170 dB re. 1 μPa and −54 (below the detection level with our setup), −54,-43,-33, and −22 dB re. 1g respectively (Figures S3B and S3C). Each stimulus was presented 5 times with a 9 s inter-stimulus interval.

Some of the highest sound intensity produced vibration artifacts in the imaging, the corresponding frames were therefore removed from the recordings. We were still able to record neural activity due to the slow dynamics of GCaMP5. A multiple regression model was fit to estimate the amplitude of the neural response. ROIs responsive to the stimulus were identified as previously stated, and only those ROIs activity was kept for further analysis. To evaluate the threshold at which neural activity was deemed significant, we estimated the null distribution of the regression coefficients by fitting neural activity in between stimulations. Regression coefficients with a value above the 95th percentile of the null distribution were considered significant.

Finally, the regression coefficients from all detected ROIs were averaged together to obtain a single number, representative of the overall brain activity at each frequency and intensity level.

Calcium imaging

Two-photon calcium imaging

Zebrafish larvae (*Huc:GcaMP5)* from 7 to 21 dpf were head-embedded in 2% low-melting agarose inside a recording chamber filled with E3 embryo medium (Figure 1A). The tail of the larva was freed from agarose and tail bouts were recorded (150 Hz) from below with a high-speed camera (*Baumer HXG20NIR*) and infra-red illumination. Neural activity was monitored using a two-photon microscope (MOM, *Sutter Instruments) controlled by Scanimage 3.8.* We used a 25x, NA 1.05 objective (*Olympus*) and a Ti:Sapphire laser (*Spectra-Physics Mai Tai DeepSee*) tuned at 920 nm. The whole hindbrain was recorded at different depths with a frame rate of 2.79 Hz. Auditory stimuli, behavior recordings and two-photon imaging were synchronized using TTL signals (*Arduino Uno*).

Selective-plane illumination microscopy

We used selective-plane illumination microscopy (SPIM) to record the neuronal activity from different optical sections of the zebrafish hindbrain, with near cellular resolution. Optical sectioning was achieved by the generation of a micrometer-thick light sheet to excite GCaMP5 from the side of the larva. The GCaMP emission was collected by a camera whose optical axis was orthogonal to the excitation plane (a 488 nm laser, Phoxx 480-200, Omicron). The laser beam was first filtered by a 488 cleanup filter (XX.F488 Omicron) and coupled to a single-mode fiber optic. The beam was expanded using a telescope (f = 50 mm, LA1131-A, and f = 150 mm, LA1433-A, Thorlabs) and projected onto two orthogonal galvanometric mirrors (HP 6215H Cambridge technology) to scan the laser beam, whose angular displacement were converted into position displacement by a scan lens (f = 75 mm AC508-075-A-ML, Thorlabs). The laser beam was then refocused by a tube lens (f = 180 mm, U-TLUIR, Olympus) and focused on the pupil of a low-NA (0.16) objective lens (UPlan SAPO 4x, NA = 0.16, Olympus) facing the specimen chamber. This arrangement yielded a 1mm-wide illumination sheet and a beam waist of 3.2 μm (1/e2). The emitted fluorescence light was collected by a high-NA water-dipping objective (N16XLWD-PF, 16x, NA = 0.8, Nikon) mounted vertically on a piezo translation stage (PI PZ222E). A tube lens (f = 180mm U-TR30IR, Olympus), a notch filter (NF03-488, to filter the laser's excitation light), a band-pass filter (FF01 525/50 Semrock) and a low-pass filter (FF01 680 SP25 Semrock, to filter the IR light) were used to create an image of the GCaMP5 emitted fluorescence on a sCMOS sensor (Orca Flash 4.0, Hamamatsu). The acquisition rate was 20 Hz.

Data analysis

Pre-processing of neural data

The acquired series of images were registered to correct for potential drifts in the XY plane using a custom script written in MATLAB which computes the cross correlations in the Fourier domain and the offset value for each frame in the dataset. We then smoothed the curve describing the offset values against time using a running average with a sliding window of 100 frames, and subtracted each offset value from this smoothed curve. This difference was then used to estimate the deviation of the position of each frame the baseline. Then, we computed the Z-scores across a sliding window of 100 frames and tagged displacements that had a Z-score over a threshold of 3. These displacement events above the threshold were then manually curated to remove movement artifacts. This procedure removed on average 2.27 ± 0.74% of the frame per larva. Since the expression of Huc:GCaMP5 is cytosolic, most of the recorded signals originate at the neuropil. We therefore decided to segment images using small hexagons that matched the size of neurons. The time series of pixel belonging to the same hexagon were averaged together. We computed the baseline fluorescence as the 8^{th} percentile in a running window of 30 s [14] to obtain the relative change of fluorescence (ΔF/F).

The same procedure was applied to pre-process the light-sheet datasets. However, since the larvae were more constrained within a capillary tube, and we recorded at a higher frame rate (20 Hz), movements of the larvae did not affect the analysis of the datasets, and therefore no frames were removed from the registered datasets.

Selection of regions of interest and sensorimotor ratio

We selected ROIs responsive to auditory stimuli of different frequencies and ROIs according to their correlation with motor behavior using a multivariate linear regression approach. We built one regressor for each frequency of the presented auditory stimuli as the convolution between the indicator function of the stimulus presentation (0 in the absence of stimulus and 1 when a stimulus was presented) and the GCaMP5 kernel (Figure S2A).

To find ROIs correlated with behavior we built one regressor for each frame around the onset of the tail movements (from 10 frames before to 10 frames after the onset of the movement for the two-photon experiments, making a total of 21 regressors, Figure S2D, and from 10 frames before to 40 frames after the onset of the movement for the light-sheet experiments, making a total of 51 regressors). The two linear models for auditory stimuli and motor behavior were fit separately on the datasets. Generally, the neural responses that

correlated with motor behavior displayed larger amounts of trial-to-trial variability compared to sensory responses. This, and the design of the linear model for motor behavior resulted in lower values for R^2 values describing motor behavior when compared to R^2 values for auditory stimuli.

In order to select ROIs responsive to the auditory stimuli or correlated with the motor behaviors, we built a null model were the stimulus timings were shifted to fall into regions of spontaneous activity, while the inter-stimulus intervals were preserved. We applied the regression analysis to the shifted regressors and obtained a null distribution for the R^2 values in 2 dimensions. Only regions of interest with a mahalanobis distance of 7 from the center of a 2D Gaussian fit to the null distribution were considered as responsive ROIs and were kept for further analysis (Figure S5). For experiments in which behavior was not recorded, we kept ROIs with a R^2 value above a threshold of 0.10 for the regression with auditory stimuli.

To determine whether a ROI was more responsive to auditory stimuli or correlated with behavior, we computed a sensorimotor ratio (SMR) based on the percentage of variance explained by the linear regression analysis: $SMR = (R^2_{mvt} - R^2_{stim}) / (R^2_{mvt} + R^2_{stim})$.

Spatial normalization

As a reference stack, we imaged the whole brain of a 7 dpf *Huc:GCaMP5* larva (132 planes) using a confocal microscope (Leica SP5) with a lateral resolution of 1.21 μm per pixel and an axial resolution of 2.98 μm per pixel. Individual optical sections of different larvae were manually registered to the confocal stack using an affine transformation. This allowed us to project the position of ROIs from different larvae into a common 3D reference space.

Density maps

To obtain the cell-density map for each frequency-tuning cluster (Figure 2D), we computed the density of ROIs in each cluster in the 3D reference space by convolving with a Gaussian kernel (sigma = 3.63 μm in the XY axis, 8.94 μm in the Z axis). We then projected the normalized maximum density along the Z and y axis, color-coded according to the cluster whose density is maximal. To compute the density along a relevant axis, we projected on this axis the number of ROIs of each cluster, and then computed the density along that axis using kernel density estimation.

Detection of the onset and the duration of Ca^{2+} transients

To compute the onset and the duration of calcium transients in the datasets acquired using the light-sheet microscope at 20 Hz, we averaged across trials the ΔF/F traces. These were then smoothed temporally using a Gaussian filter (σ = 150 ms) to remove noise in the signal. The onset was computed as the time point where the second derivative of the smoothed traces was maximal. The duration was defined as the full width at half-maximum of the smoothed traces. For this purpose we used a linear interpolation.

Pre-processing of behavioral data

Videos of the tail of the larva were analyzed as previously described in Olive et al. [42]. Briefly, the tail was segmented and two ellipses fit to the head and tail of the larva. The tail deflection was defined as the inverse of the average distance between all the pixels in the larva and the intersection of the minor axis of the two ellipses. To obtain a dimensionless value, the result was multiplied by the length of the larva at rest.

Analysis of motor behavior

Movements that occurred in a 500 ms time window after the onset of an auditory stimulation were considered as elicited by the stimulation. To validate this approach, we used a permutation-based approach. We counted the number of stimuli followed by at least one tail bout in a 500 ms time window and compared this number to a null model where the onset of movements was shuffled but the inter-bout interval distribution was kept intact.

Clustering of tuning curves and clustering validation

To calculate the frequency tuning curves of each ROI, we computed for each presented frequency the average ΔF/F within a 2 s time window starting at the onset of the stimulus. This was further averaged across the different trials. To cluster the frequency tuning curves, we pooled the tuning curves from all ROIs responding to the auditory stimuli from all animals. The tuning curves were normalized so that the minimum value was set to zero and the maximum to one, which allows clustering together tuning curves of similar shape but different amplitudes. We used the k-means algorithm with euclidean distance to cluster the tuning curves.

To validate the clustering solution, we used a set of convergent approaches. We computed two clustering indices, the Calinski-Harbasz index which is based on the ratio of between and within-cluster variance, and the Silhouette index, which describes how similar each observation is to observations in its own cluster, when compared to observation in other clusters.

The Calinski-Harabasz criterion is defined as:

$$CH(k) = \frac{SS_B}{SS_W} \times \frac{N-k}{k-1}$$

where k is the number of clusters, and N is the number of observations. The between-cluster variance is defined as:

$$SS_B = \sum_{i=1}^{k} n_i \times \|m_i - m\|^2$$

where n_i is the number of observations in cluster i, m_i is the centroid of cluster i, m is the overall mean of the data. The within-cluster variance is defined as:

$$SS_W = \sum_{i=1}^{k} \sum_{x \in c_i} \| x - m_i \|^2$$

where x is a data point, c_i is the ith cluster, and m_i is the centroid of cluster i.

The silhouette index for one observation i is defined as:

$$S_i = \frac{b_i - a_i}{max(a_i, b_i)}$$

where a_i is the average distance from the ith point to the other points in the same cluster as i, and b_i is the minimum average distance from the ith point to points in a different cluster, minimized over clusters. The silhouette value ranges from –1 to 1. A high silhouette value indicates that i is well-matched to its own cluster, and poorly matched to other clusters.

We also used a hierarchical clustering approach, using Ward's method, which iteratively merges clusters together to minimize the overall within-cluster variance. Hierarchical clustering also yields a dendrogram, which describes the structure of the clustering solution in terms of distance between clusters. The distance between two clusters A and B is computed as:

$$\Delta(A, B) = \frac{n_A n_B}{n_A + n_B} \| m_A - m_B \|^2$$

where n_A is the number of points in cluster A, n_B is the number of points in cluster B, m_A is the centroid of cluster A and m_B is the centroid of cluster B. A large distance between clusters indicates a high cost for merging the clusters in terms of overall within-cluster variance.

Finally, we also used principal component analysis. We inspected the distribution of scores in PC space, to find signs of multimodality. Gaussian-mixture models with 2 components were fit to the distribution of scores for PC1 and PC2 to find the value that best separated between components. We used these thresholds as a linear separation to classify the data in 4 groups and compare it with our k-means clustering results.

Presenting auditory stimuli with higher frequency resolution (150 – 300 Hz using frequency steps of 10 Hz) showed similar clustering results suggesting that the low dimensionality of frequency representation in the larva's nervous system is not due to the type of auditory stimuli used.

High speed recording of behavior

To characterize the delay between the onset of the acoustic stimulation and the onset of behavior, we recorded the behavior of the larvae using a high-speed camera at 1000 Hz (Baumer HXG20NIR) with infrared illumination. To synchronize the video recordings with the auditory stimuli (500 ms broadband noise between 250 Hz and 1000 Hz), we triggered the camera with a National Instruments NI PCI-6711 card. The resulting videos were then analyzed manually to determine the onset of behavior. We used 3 types of stimulation: 0dB (no sound), 155dB and 170dB re. 1 μPa, with an inter-stimulus interval of 30 s. For the strong stimulus, the histogram of delay was multimodal, we estimated the statistics of each component separately using a Gaussian mixture model.

Lateral line ablation

To evaluate the contribution of the lateral line system to the auditory neural responses, we chemically ablated the lateral line using neomycin. Larvae were incubated during one hour in a 200 μM neomycin solution (Sigma) in E3 medium, rinsed for one hour in E3 medium and placed under the microscope for recording [14, 48]

Registration to the z-brain atlas

Our reference brain (7 dpf Huc:GCaMP5 larva, 132 planes) was registered against the Elavl3:GCaMP5 brain in the z-brain atlas [39] using the Computational Morphometry Toolkit (CMTK) [49]. We used the command:

cmtk registration –initial initial.xform -v –dofs 6,9,12 -o affine.xform reference.nrrd sample.nrrd to produce the initial affine transformation and cmtk warp -v –registration-metric nmi –jacobian-weight 1e-5 –fast -e 16 –grid-spacing 100 –energy-weight 1e-1 –refine 2 –coarsest 4 –ic-weight 0 –accuracy 0.5 –output-intermediate -o warp.xform –initial affine.xform reference.nrrd sample.nrrd, to perform the final elastic registration.

QUANTIFICATION AND STATISTICAL ANALYSIS

Whenever we could not assume a normal distribution of the data, the statistical inference was made using a non-parametric framework: permutation-based tests, Wilcoxon rank sum test for independent samples, or Wilcoxon signed rank test for paired samples.

In the cases where multiple testing were performed, we used Bonferonni correction (p values are adjusted by multiplying by the number of tests performed) to control for the number of false positives.

DATA AND CODE AVAILABILITY

Raw data and codes from the current study were not deposited into a public repository due to the large size, but are available from the Lead Contact upon request.

Current Biology, Volume *29*

Supplemental Information

Sensorimotor Transformations in the Zebrafish Auditory System

Martin Privat, Sebastián A. Romano, Thomas Pietri, Adrien Jouary, Jonathan Boulanger-Weill, Nicolas Elbaz, Auriane Duchemin, Daphne Soares, and Germán Sumbre

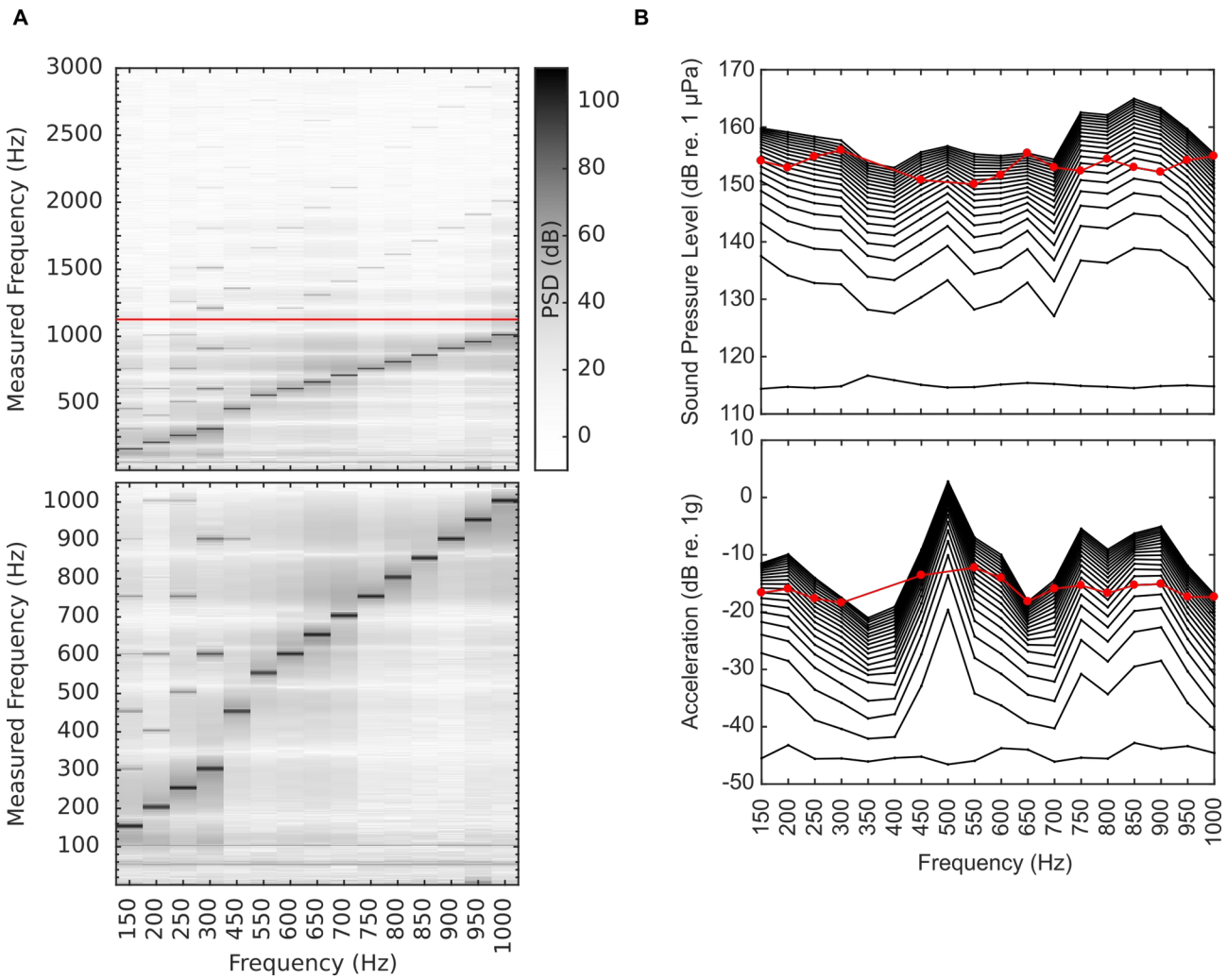

Figure S1. Acoustic calibration of the recording chamber. Related to Figure 1.
(A) The spectral content of acoustic stimulation was controlled to ensure that most of the power lies in the fundamental frequency. Top: power spectrum between 1 and 3000 Hz; bottom: close-up between 1 and 1000 Hz.
(B) Pure tones with frequency ranging from 150 to 1000 Hz were used to stimulate the larvae. The recording chamber was calibrated using a hydrophone and a suspended accelerometer to control sound pressure levels and particle acceleration across frequencies. The larvae were stimulated with a sound pressure level of 155 dB re. 1µPa (measured at 2 cm from the speaker due to the shape of the chamber), and a particle acceleration close to -15 dB re. 1g (red lines).

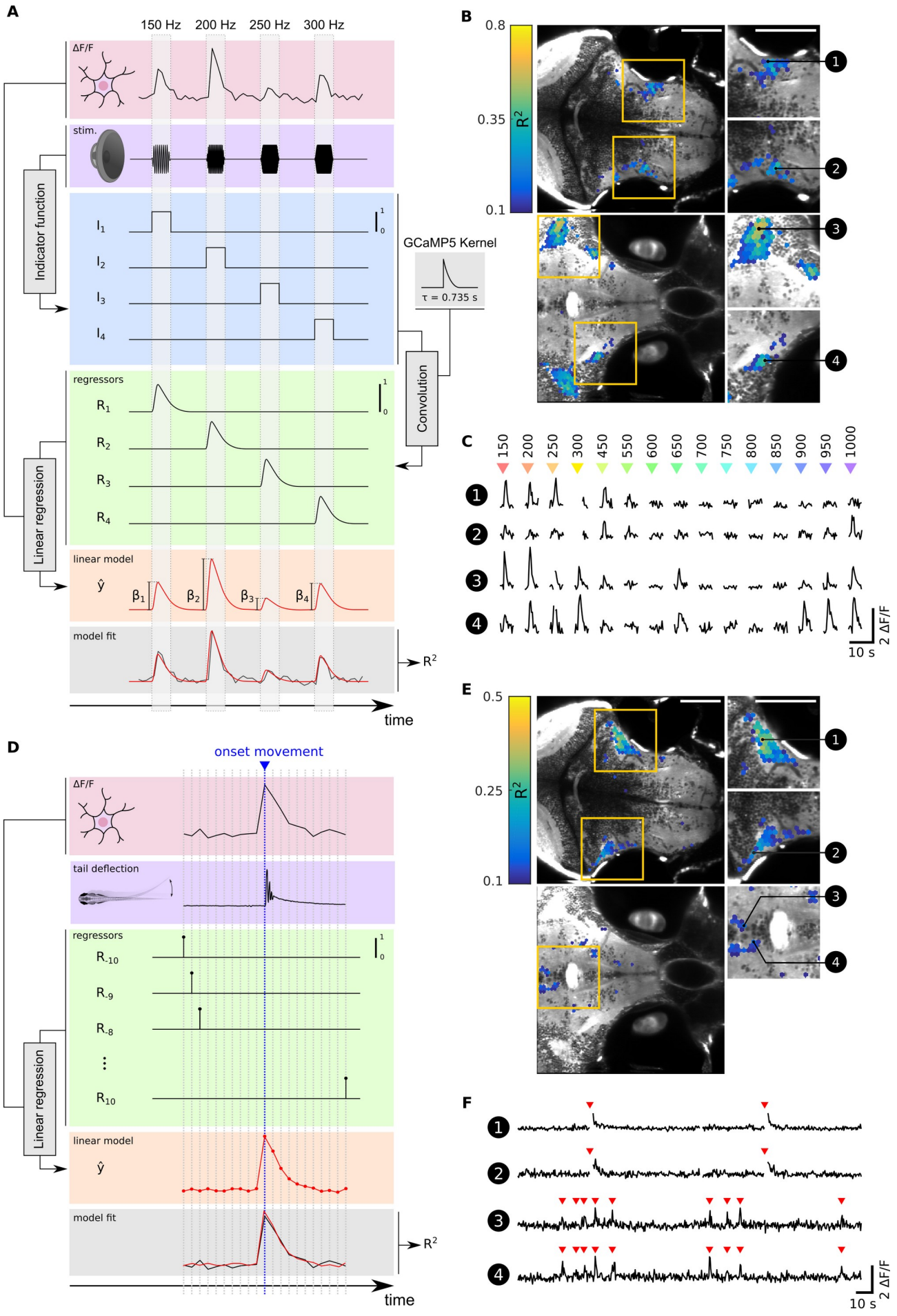
A
150 Hz
200 Hz
250 Hz
300 Hz
ΔF/F
stim.
Indicator function
I1
I2
I3
I4
GCaMP5 Kernel
τ = 0.735 s
Convolution
regressors
R1
R2
R3
R4
Linear regression
linear model
ŷ
β1
β2
β3
β4
model fit
R2
time
B
0.8
0.35
0.1
R2
1
2
3
4
C
150
200
250
300
450
550
600
650
700
750
800
850
900
950
1000
10 s
2 ΔF/F
D
onset movement
ΔF/F
tail deflection
regressors
R-10
R-9
R-8
R10
Linear regression
linear model
ŷ
model fit
R2
time
E
0.5
0.25
0.1
R2
1
2
3
4
F
10 s
2 ΔF/F

Figure S2. Detection of regions of interest correlated with acoustic stimuli and behavior. Related to Figure 1.

(A) Linear regression model used to detect regions of interest whose activity is correlated with acoustic stimuli. For each frequency presented, a regressor was build as the convolution between an indicator function (which takes the value 1 when the stimulus is presented and 0 everywhere else), and the calcium impulse response function for GCaMP5 (GCaMP5 kernel). The goodness of fit was measured by the percentage of variance explained by the model (R^2).

(B) Example topography of the neural responses to acoustic stimuli for two optical sections, in the octaval nuclei (top), and in the torus semicircularis (bottom). The color code reflects how well the variance in the neural activity is explained by the regression model. Right panels, close-up on the regions outline by the yellow squares. Scale bar, 100 µm. Activity traces for regions of interest 1 to 4 are represented in c).

(C) Single-trial traces of neural activity for regions of interest 1 to 4 defined in b) induced by 1s acoustic stimulation. Arrowheads: stimulus onset and corresponding frequency in Hz. Breaks in the traces are discarded frames due to movement artifacts.

(D) Linear regression model used to detect regions of interest whose activity is correlated with behavior. One regressor was used for each frame in a 10 frames window around movement onset.

(E) Example topography of the neural activity associated with movements of the tail. Activity traces for regions of interest 1 to 4 are represented in (F).

(F) Traces of neural activity for regions of interest 1 to 4 defined in (E). Red arrowheads: onset of tail movements.

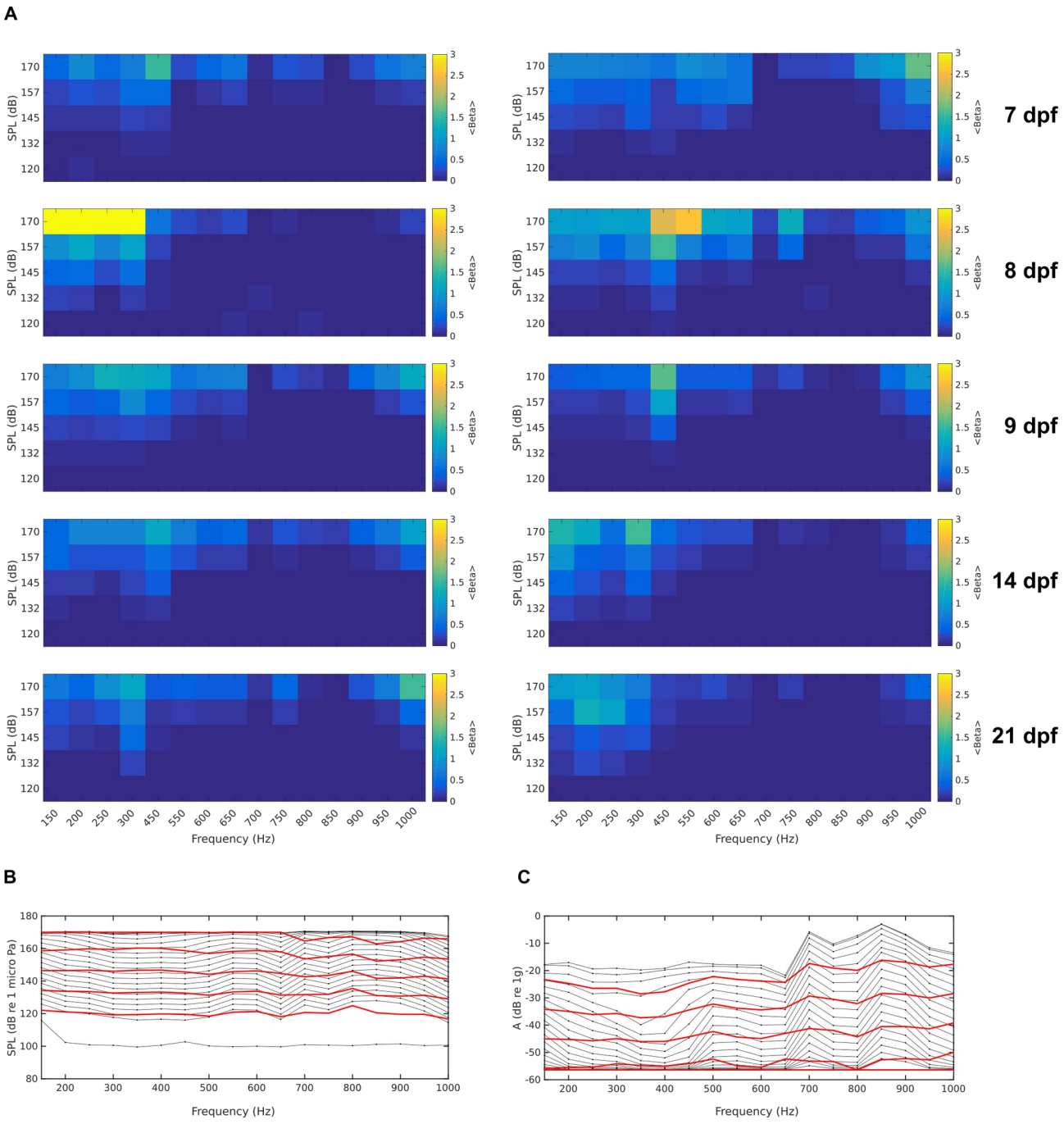

Figure S3. Audiograms at different developmental stages and calibration of the recording chamber. Related to Figure 3.

(A) Two examples of audiograms of individual larvae at different developmental stages from 7 to 21 dpf.

(B-C) The recording chamber was calibrated to deliver acoustic stimuli with 5 intensity levels equally spaced and equalized over frequencies for sound pressure level (B), and particle acceleration (C). Black curves: the recorded sound pressure and acceleration for each frequency and for a given voltage stimulus. Red curves: the calibrated voltages for the different frequencies to obtain homogeneous sound pressure levels and accelerations across the whole range of tested frequencies.

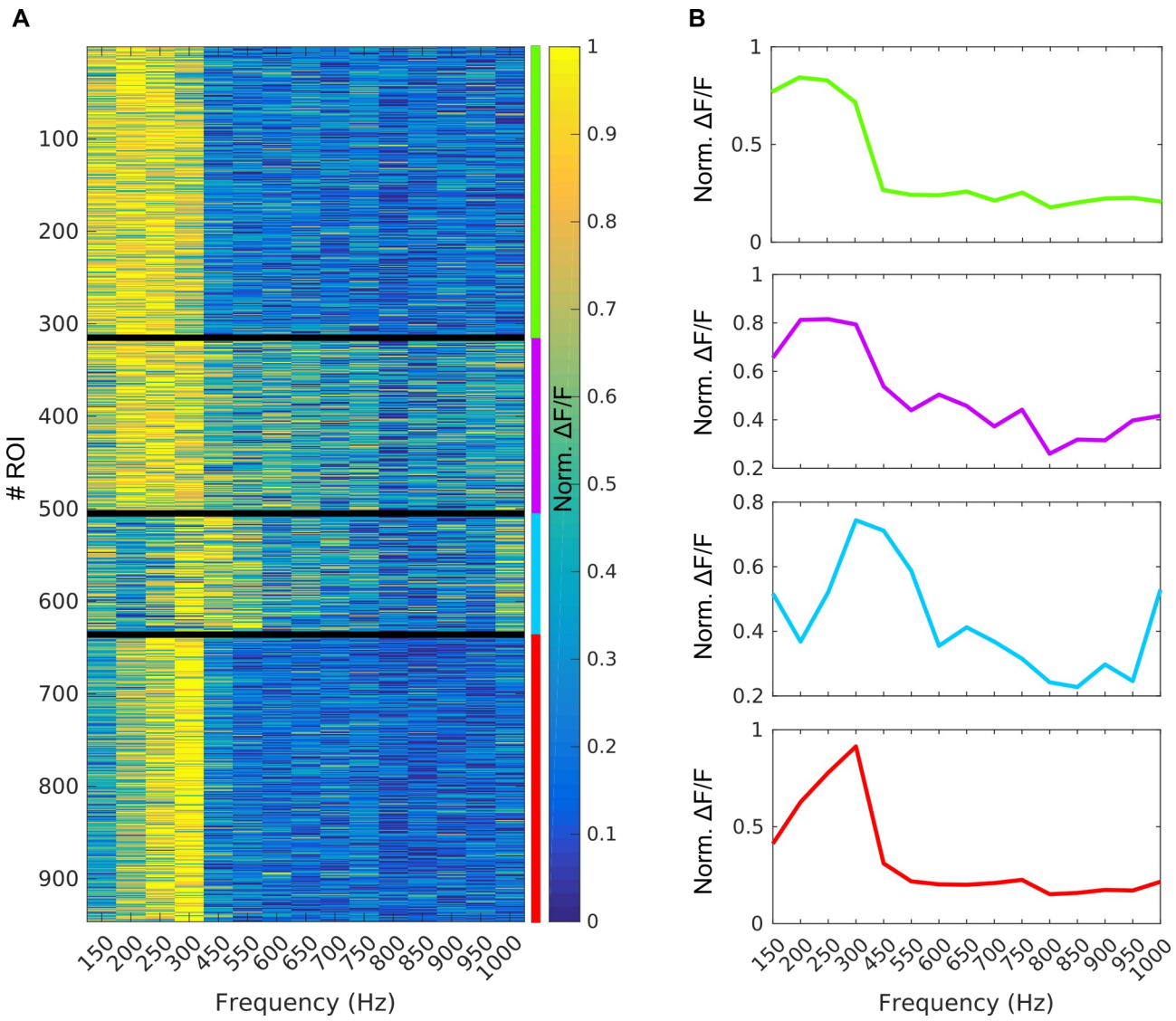

Figure S4. Auditory induced neuronal responses are unaffected by lateral line ablation with neomycin. Related to Figure 2.
(A) Frequency tuning curves of 8 dpf larvae (N=7) exposed for 1 hour to neomycin to ablate the lateral line, grouped in 4 clusters using k-means clustering algorithm.
(B) Average tuning curve for each cluster.

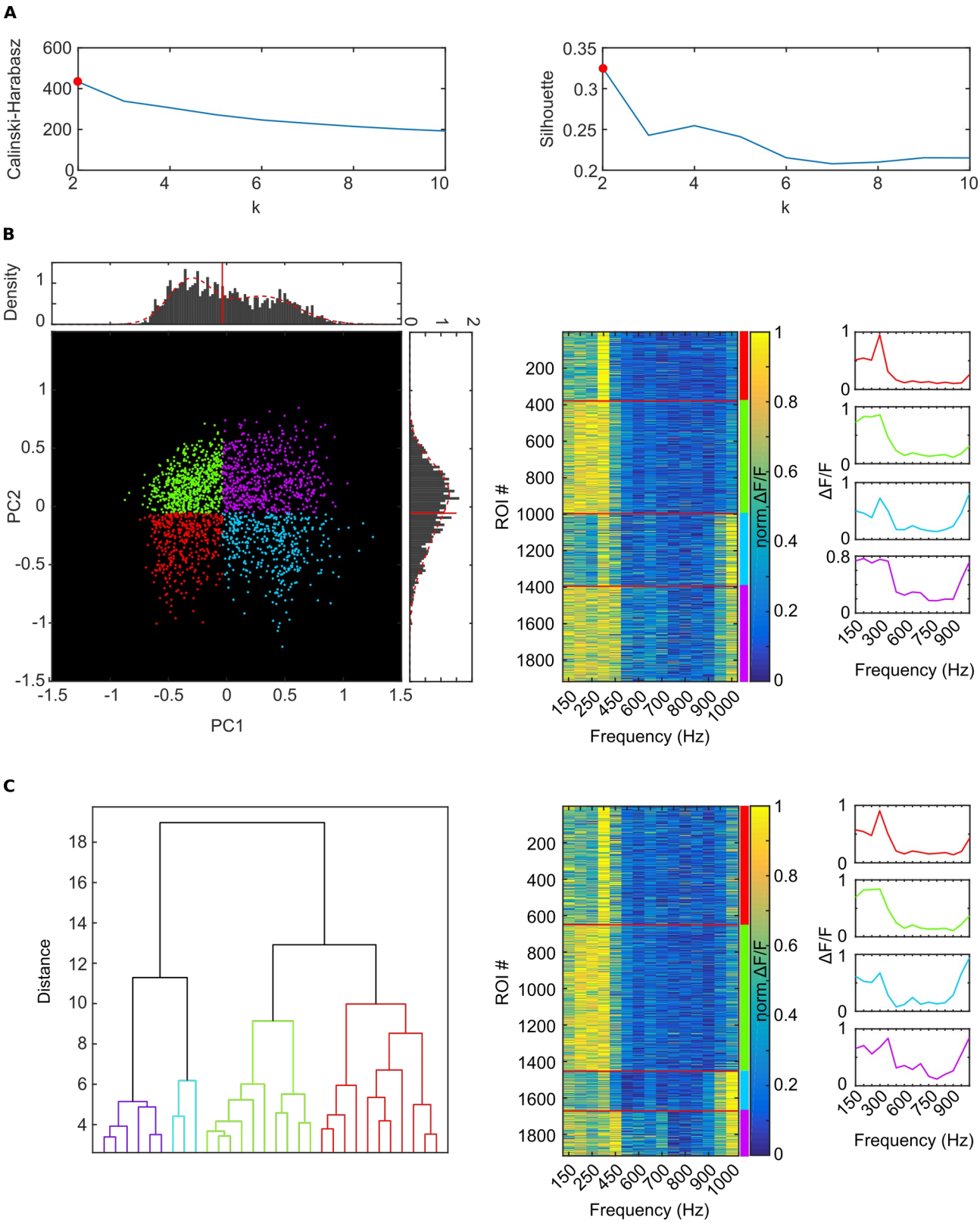

Figure S5. Validation of tuning curves clustering. Related to Figure 2.
(A) Calinski-Harabasz and Silhouette indexes for clustering solution with 2 to 10 clusters (k). Red dot: optimal value.
(B) Left: Tuning curves projected in principal component (PC) space. A two-component Gaussian mixture model was fit to the distribution of scores of PC1 and PC2 (red dotted line), and a threshold was selected as the best separation between the two components for each PC (red bar). Tuning curves were color coded according to their position respective to these two thresholds. Right: ROIs tuning curves organized according to the thresholds set on PC1 and PC2.

(C) Hierarchical clustering using euclidean distance and Ward's variance criterion. Left: simplified dendrogram of the hierarchical clustering solution, Right: ROIs tuning curves organized according to the hierarchical clustering solution. Note the similarity with those obtained using k-means (Figure 2B).

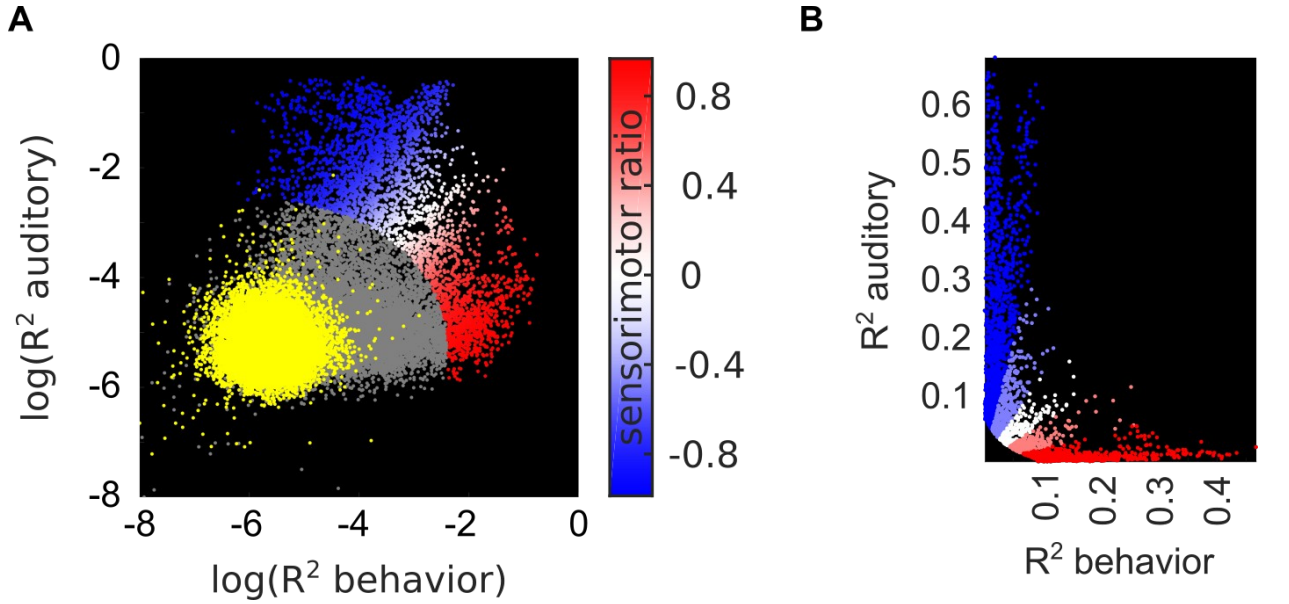

Figure S6. Distribution of the percentage of variance explained by the linear models. Related to Figure 6.

(A) A null model was obtained by shifting all the fluorescence time series by the same amount, which preserves the temporal structure of the data but destroys the association with stimulus and behavior. Distribution of R^2 for the null model are shown in yellow. A two-dimensional Gaussian, was fit to the null model, ROIs were deemed responsive either to the stimulus or behavior if they had a Mahalanobis distance of 7 with respect to the mean of the Gaussian fit to the null model. Those responsive ROIs are color-coded based on the value of their sensorimotor ratio (STAR Methods).

(B) Sensorimotor ratio bins used in Figure 6A.

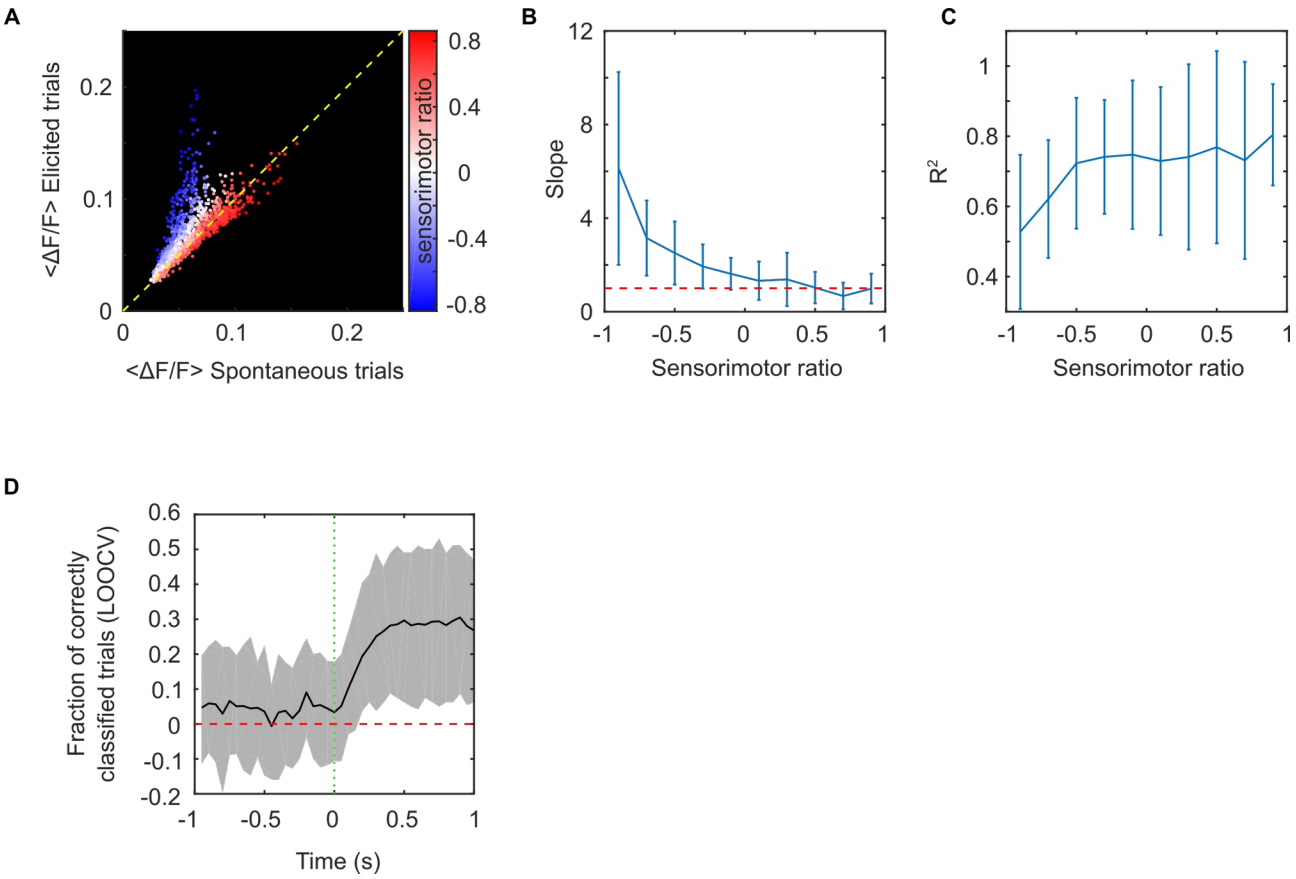

Figure S7. Motor networks display similar activity during self-generated and auditory elicited behavior and spontaneous activity preceding the auditory stimulus fails to predict behavior. Related to Figure 7.

(A) Example of ΔF/F averaged over elicited trials versus ΔF/F averaged over spontaneous trials for one larva. ROIs are color coded according to their sensorimotor ratio. Yellow doted line represents the time where activity was the same for spontaneous and elicited trials.

(B) A linear regression was fit for 10 bins of the sensorimotor ratio between ΔF/F averaged over elicited trials and ΔF/F averaged over spontaneous trials (27 larvae). The average slope and standard deviation of the linear fit are plotted against the centers of the sensorimotor ratio bins. Red dotted line: slope = 1.

(C) Average percentage of variance explained by the linear models and standard deviation versus sensorimotor ratio.

(D) Fraction of trials correctly classified (tail movement vs no tail movement) using linear discriminant analysis on the neural activity around the onset of auditory stimulation (estimated using leave one out cross-validation). Chance level was estimated by disrupting the association between neural activity and behavior (100 permutations of the class labels) and subtracted from the fraction of trials correctly classified to obtain the fraction of trial correctly classified above chance level. Red dashed line : chance level. Green dotted line: onset of auditory stimulus. Gray area: 5^{th} to 95^{th} percentile of the distributions obtained by shuffling the labels.